

**Fabrication, Characterization,
And Deformation of 3D
Structural Meta-Materials**

Thesis by

Lauren C. Montemayor

In Partial Fulfillment of the Requirements

for the Degree of

Doctor of Philosophy



CALIFORNIA INSTITUTE OF TECHNOLOGY

Pasadena, California

2016

(Defended June 23, 2015)

© 2016

Lauren C. Montemayor

All Rights Reserved

Acknowledgements

I would like to acknowledge my advisor, Professor Julia Greer, for all of her support and guidance during my time at Caltech. I have learned so much from her, not only how to do great science but also how to spread enthusiasm for my work throughout the community. I am thankful for the numerous opportunities to present at conferences and I appreciate her active involvement in my projects from start to finish.

I would like to thank Professors Dennis Kochmann, Michael Ortiz, Sergio Pellegrino, and Guruswami Ravichandran for being a part of my thesis and/or candidacy committees. Dr. Yong-Wei Zhang and Dr. Wei Hin (Mark) Wong at the Institute for High Performance Computing have been fantastic collaborators and it was great to work closely with them. I am grateful for the many opportunities to discuss my work with Professors Lorenzo Valdevit (UC Irvine), John Hutchinson (Harvard), Norman Fleck (Cambridge), Katherine Faber (Caltech), and Wolfgang Knauss (Caltech). I am thankful to have frequent meetings/Skype calls with so many influential contributors to the field of mechanics and it has made my time at Caltech an invaluable learning experience. I would like to acknowledge the National Science Foundation Graduate Fellowship Research Program for the financial support that allowed me to do this work.

I would also like to thank Dr. Zach Aitken and Prof. Dongchan Jang for their help in the TEM sample preparation and analysis. Thanks to Kermit Parks at Nanomechanics, Inc. for working with me to develop a new testing algorithm for the nanolattices. The fantastic staff at the Kavli Nanoscience Institute at Caltech provided crucial support and infrastructure, especially Melissa Melendes and Matt Sullivan. I would also like to thank

all of the staff at Nanoscribe GmbH, especially Gerhard Balthasar, for help in making these unique structures. I also thank Prof. Morteza Gharib for encouraging me early in my time at Caltech to find a project I loved.

A huge thanks to my fantastic Women Mentoring Women mentors, Dr. Suzanne Kern and Dr. Betar Gallant, for helping me through some of the roughest times in grad school and for always being available to talk. I'd also like to thank Felicia Hunt, Portia Harris, and the staff at the Diversity Center for their endless support during my time at Caltech and for all the great programs/events.

Rachel, Viki, Wendy, Zach, David, Ottman, Alessandro, and Lucas: thanks so much for making the lab such a fun place to work and for always being willing to help me think through technical challenges. I have learned so much from our discussions and you have made my time in the Greer group great. Pratyush, Patrick, Elisabeth, Tucker, Joel, and other alpine club friends: thanks for teaching me to climb and for sharing your love of the mountains; it was one of the best things I learned in grad school. Masha, Jackie, Melodie, Hannah, Tamar, Anna, and Katy: thank you for being great roommates/friends and for all the impromptu wine nights. Thanks to Tima(shenko) for being the best hiking buddy.

Lastly, thanks to my family – especially my brother, Dr. Eric Montemayor, for sending me so many journal articles, proofreading proposals, and for being supportive of me during my time in grad school.

Abstract

Current technological advances in fabrication methods have provided pathways to creating architected structural meta-materials similar to those found in natural organisms that are structurally robust and lightweight, such as diatoms. Structural meta-materials are materials with mechanical properties that are determined by material properties at various length scales, which range from the material microstructure (nm) to the macro-scale architecture (μm – mm). It is now possible to exploit material size effect, which emerge at the nanometer length scale, as well as structural effects to tune the material properties and failure mechanisms of small-scale cellular solids, such as nanolattices.

This work demonstrates the fabrication and mechanical properties of 3-dimensional hollow nanolattices in both tension and compression. Hollow gold nanolattices loaded in uniaxial compression demonstrate that strength and stiffness vary as a function of geometry and tube wall thickness. Structural effects were explored by increasing the unit cell angle from 30° to 60° while keeping all other parameters constant; material size effects were probed by varying the tube wall thickness, t , from 200nm to 635nm, at a constant relative density and grain size. In-situ uniaxial compression experiments reveal an order-of-magnitude increase in yield stress and modulus in nanolattices with greater lattice angles, and a 150% increase in the yield strength without a concomitant change in modulus in thicker-walled nanolattices for fixed lattice angles. These results imply that independent control of structural and material size effects enables tunability of mechanical properties of 3-dimensional architected meta-materials and highlight the importance of material, geometric, and microstructural effects in small-scale mechanics.

This work also explores the flaw tolerance of 3D hollow-tube alumina kagome nanolattices with and without pre-fabricated notches, both in experiment and simulation. Experiments demonstrate that the hollow kagome nanolattices in uniaxial tension always fail at the same load when the ratio of notch length (a) to sample width (w) is no greater than $1/3$, with no correlation between failure occurring at or away from the notch. For notches with $(a/w) > 1/3$, the samples fail at lower peak loads and this is attributed to the increased compliance as fewer unit cells span the un-notched region. Finite element simulations of the kagome tension samples show that the failure is governed by tensile loading for $(a/w) < 1/3$ but as (a/w) increases, bending begins to play a significant role in the failure. This work explores the flaw sensitivity of hollow alumina kagome nanolattices in tension, using experiments and simulations, and demonstrates that the discrete-continuum duality of architected structural meta-materials gives rise to their flaw insensitivity even when made entirely of intrinsically brittle materials.

Table of Contents

Acknowledgements.....	3
Abstract.....	6
List of Figures and Tables.....	9
Chapter 1: Introduction to Structural Meta-Materials.....	11
1.1 Overview of Architected Materials and Material Size Effects	11
1.2 Fabrication Technique: Microlattices via Polymer Wave-Guides	14
1.3 Fabrication: Microlattices via Micro-Stereolithography	17
1.4 Fabrication: Nanolattices via Direct Laser Writing Two-Photon Lithography (DLW TPL)	18
Chapter 2: Design and Fabrication of Hollow Rigid Nanolattices Via Two-Photon Lithography	26
2.1 Fabrication of Polymer Nanolattices via TPL DLW.....	26
2.2 Conformal Sputtering of Nanolattices.....	29
2.3 O ₂ Plasma Etching to Create Hollow Nanolattices	30
2.4 Calculating Relative Density of Hollow Nanolattices.....	32
2.5 Conclusions	34
Chapter 3: Mechanical Response of Hollow Metallic Nanolattices: Combining Structural and Material Size Effects	35
3.1 Introduction.....	35
3.2 Background: Cellular Solids	37
3.3 Background: Material Size Effects.....	41
3.3.1 Uniaxial Deformation	41
3.3.2 Beyond Nano-pillars: Deformation under Complex Stress States.....	42
3.4 Experimental Methods	43
3.5. Results	46
3.5.1 Structural Effects.....	46
3.5.2 Material Size Effects.....	49
3.6 Discussion	51
3.6.1 Critical Stress Criteria: Euler Buckling or Yielding of Lattice Struts.....	51
3.6.2 Structural Effects.....	57
3.6.3 Material Size Effects	61
3.7 Conclusions	64
Chapter 4: Insensitivity to Flaws Leads to Damage Tolerance in Brittle 3D Architected Meta-Materials	66
4.1 Introduction.....	66
4.2 Fabrication of Hollow Kagome Tension Samples.....	68
4.3 In-Situ Uniaxial Tension Experiments and Simulations	71
4.4 Results	73
4.5 Discussion	76
4.5 Conclusions	83
Chapter 5: Summary and Future Work/Outlook of Structural Meta-Materials	85

Appendices	88
Appendix A: Laser Power Exposure Test Matrix	88
Appendix B: Representative Images of Etched and Non-Etched Samples	89
Appendix C: Calculation of Stiffness for Grip and Test Gauge Sections	90
Appendix D: Elastic Blunting Phenomena in 3D Hollow Kagome Nanolattices	93
Appendix E: Peak Load for Variation in Wall Thicknesses	94
References	95

List of Figures and Tables

Figure 1: Representative images of structural meta-materials	14
Figure 2: Summary of fabrication methodologies for structural meta-materials.....	15
Table 1: Summary of structural meta-materials in terms of fabrication method, relative density, strength, and modulus.....	24
Figure 3: Fabrication process to create hollow rigid nanolattices.....	27
Figure 4: CAD model and SEM images of fabricated structures for three different nanolattice geometries.	30
Figure 5: SEM images of the hollow structures for the three lattice geometries.....	31
Figure 6: SEM images of representative nanolattices for different relative densities and geometries.....	33
Figure 7: Hierarchically structured materials combine structural and material size effects to enhance material properties and provide opportunities to create new materials that outperform existing materials.....	36
Figure 8: Schematic of relevant geometric parameters on a nanolattice unit cell (A) and TEM image showing columnar grain structure of tubes with grain size on the order of 50nm (B).....	39
Figure 9: Representative images of the Au coating in a 60° nanolattice with a wall thickness of ~661nm.....	45
Figure 10: SEM image of octahedron nanolattices with lattice angles from 30° to 60°, as well as representative stress- strain curve for each sample; an open circle denotes 0.2% yield stress of the structure.....	47
Figure 11: Calculated yield stress and modulus values for lattices with angles ranging from 30° to 60°.	48
Figure 12: SEM image of 45° octahedron nanolattices with t ranging from 200 to 635nm, as well as representative stress-strain curve for each sample; an open circle denotes 0.2% yield stress of the structure.	49
Figure 13: Calculated yield stress for both 45° and 60° octahedron nanolattices.	50
Table 2: Relevant average geometric parameters, as well as threshold stress values for both yielding and Euler buckling, for all samples.....	54
Table 3: Average measured and predicted yield stresses and modulus for the fabricated samples.....	56

Figure 14: A) Modulus vs. Sine of lattice angle according to Eqn. 4; B) Yield stress vs. sine of lattice angle according to Eqn. 5.....	59
Figure 15: TEM bright field image showing pores between grains as viewed through a section of a nanolattice wall where the wall thickness is $\sim 200\text{nm}$	62
Figure 16: A) Ion channeling (sample at 52° tilt) and B) TEM images of a $\sim 2\mu\text{m}$ thin n-Au film showing columnar grain structure with multiple grains spanning the film thickness.	63
Figure 17: Representative notched nanolattice tensile specimens, designed in Solidworks (A) and as-fabricated samples (E).	70
Figure 18: Representative load-displacement curve for un-notched (A) and notched (B) kagome nanolattices in uniaxial tension.....	74
Figure 19: Comparison of finite element and experimental data for $4\mu\text{m}$ kagome lattices in uniaxial tension.....	75
Figure 20: Finite element simulations show that the highest local Von Mises stress concentrations within the nanolattice occur at the nodes for both the notched and un-notched specimens. Red boxes denote the plane where failure occurs in (B) and (E)..	77
Figure 21: Stress at failure vs. the notch length to unit cell size ratio.	79
Figure 22: Contour plots of von Mises stress distributions in kagome lattice at a nominal strain of $\epsilon_y = 0.003$ for $(a/w) = 0, 0.11$ and 0.35	81
Figure 23: Small -scale explosions are observed when the laser power is sufficiently high.	88
Figure 24: Representative images of polymer etching using different SEM voltages; the red dotted line indicated the etch front of the O_2 plasma in the octet-truss head.....	89
Figure 25: Engineering stress-strain curve for compressive stiffness of 54.7° 3D kagome nanolattices.....	91
Figure 26: No elastic crack tip blunting is localized near the crack tip for the 3D kagome nanolattice plates; all deformation in the x-direction is localized near the middle of the sample at the moment prior to failure.....	93
Figure 27: Variations in wall thickness give rise to higher peak loads.	94

Chapter 1: Introduction to Structural Meta-Materials

Adapted from:

Montemayor, L.C., Chernow, V. F., Greer, J. R., “Materials By Design: Using Architecture in Materials Design to Reach New Material Property Spaces”. *MRS Bulletin (Invited)*, (2015). In

Review

1.1 Overview of Architected Materials and Material Size Effects

The concept of architecture has been used for many years to improve the efficiency of large engineered structures, such as The Great Pyramid of Giza and the Eiffel Tower, which are two notable examples of structures with vastly different architecture. The Great Pyramid is analogous to common bulk engineering materials while the Eiffel Tower is analogous to structural meta-materials, where the lattice-based architecture spans length scales down to the material microstructure. Structural meta-materials gain their unique properties from the hierarchical ordering of length scales within the material, from the microstructure of the constituent material to the large-scale structural ordering of the architecture. The emergence of *material size effects* at the nanoscale, a field that has been extensively researched and ubiquitously demonstrated in the last decade, shows that as the external dimensions of materials are reduced to the nanoscale, their mechanical behavior changes. For example, some materials can become stronger¹⁻⁹, weaker¹⁰⁻¹², or undergo brittle-to-ductile transition^{2,13-16} at room temperature depending on the microstructure of the constituent material. The behavior and properties of these structural meta-materials

can no longer be defined exclusively by the constituent material properties or by the structure, or architecture; instead these structural meta-materials must be treated as monolithic-like materials with their own unique properties that stem from the linked behavior of the material and the structure at small dimensions.

Architecture has been used widely in a variety of engineering applications to create structures that more efficiently carry load while using less raw material compared to brick-and-mortar approaches. Macro-scale cellular solids have been studied for many years experimentally, computationally, and in theory, and have assumed that the properties of the constituent solid are constant, with the geometry being the primary tunable parameter¹⁷⁻²⁶. Structural meta-materials extend this concept of architecture to multiple length scales, even down to the material microstructure, on the order of nanometers, where materials exhibit size effects and make it possible to tune the properties of the constituent material. The relationship between extrinsic material size and material properties has been extensively studied over the last decade, and it has been observed that, for sub-micron scale cylinders under uniaxial loading, the mechanical properties of materials deviate from their bulk counterparts¹⁻¹⁶. For example, the yield strength of metallic single crystals with micron and sub-micron dimensions increases in a power law fashion with size reduction; this phenomenon is referred to as a *smaller is stronger* size effect¹⁻⁹. For example, single crystalline Au nano-pillars, with external diameters of 400nm, under compression had yield strengths of 550 MPa, a value a factor of 18 higher than that of the same materials with macro-scale dimensions³. One explanation for this strength increase is hardening by dislocation starvation whereby the existing mobile dislocations within the crystal annihilate at the available free surfaces and new dislocations have to be nucleated to

facilitate further plasticity, which requires higher applied loads³. Same metals with nanocrystalline microstructure exhibit the opposite *smaller is weaker* size effect, which stems from the easier activation of grain boundary sliding in surface-dominated samples like nano-pillars⁶. Materials with homogenized microstructure at the nanometer level, such as metallic glasses, exhibit a *brittle to ductile* transition at room temperature, whereby these brittle materials are capable of an extensive ~20% deformability in tension when sample dimensions are reduced to ~100nm¹⁴. These examples demonstrate that the combination of the nano-scale extrinsic dimensions and atomic-level microstructure is crucial to understanding and predicting the mechanical behavior of small-scale materials.

The gained ability to tune material properties in sub-micron volumes can be exploited by employing architecture to use micron to nanometer building blocks to create larger structures while retaining the lucrative properties offered by nanomaterials. Stochastic foams, such as nanoporous gold shown in **Figure 1a**, have been explored as a possible vehicle to proliferate material size effects onto larger scales but are ultimately very limited in the types of structural architecture they can create and have poor scaling of strength with relative density because of the lack of ordering. Significant efforts have recently been dedicated to developing nanolattices with precisely controlled geometries that can be used to create exceptionally lightweight, strong, and tough meta-materials . Control of the 3-dimensional lattice geometry has been made possible by advances in micro- and nano-fabrication techniques, ranging from polymer wave-guides, to micro-stereolithography, to direct laser writing two photon lithography (DLW TPL) techniques³³⁻

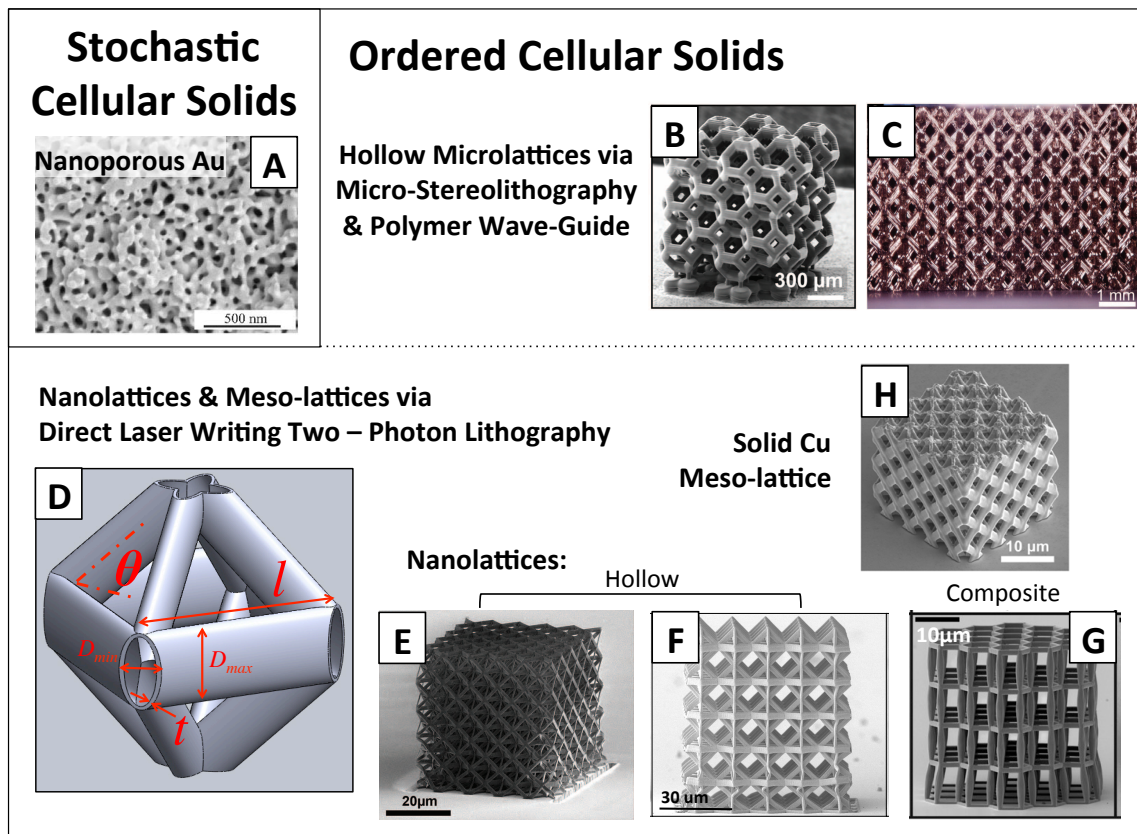


Figure 1: Representative images of structural meta-materials Nanoporous Au (A), Hollow microlattices(B, C) and Hollow Au/Ceramic nanolattices (E, F, G), and Solid meso-lattices(H). A representative unit cell is also shown (D) to denote the geometric length scales within the nanolattice meta-materials. (Figures reproduced from the following references: A²⁷, B²⁸, C²⁹, D³⁰, E³¹, F³⁰, G²⁸, H³²)

The following sections provide an overview of some of the existing 3-dimensional architected materials as a function of their fabrication technique, and their mechanical properties and densities.

1.2 Fabrication Technique: Microlattices via Polymer Wave-Guides

The microlattice shown in **Figure 1c** is a cellular solid developed by HRL Laboratories with overall dimensions on the order of centimeters or larger and with densities as low as $\rho = 0.9 \text{ g/cm}^3$, which places it into the ultra-lightweight regime ($\rho < 10 \text{ g/cm}^3$)²⁹. These microlattices are composed of hollow metallic struts with widths on the

order of 100-500 μm and lengths of 1-4mm; the wall thickness of the hollow cylindrical struts is on the order of 100-500nm²⁹. These microlattices are made using a polymer wave-guide technique that allows for macro-scale sheets to be made almost instantaneously, as shown in **Figure 2a**.

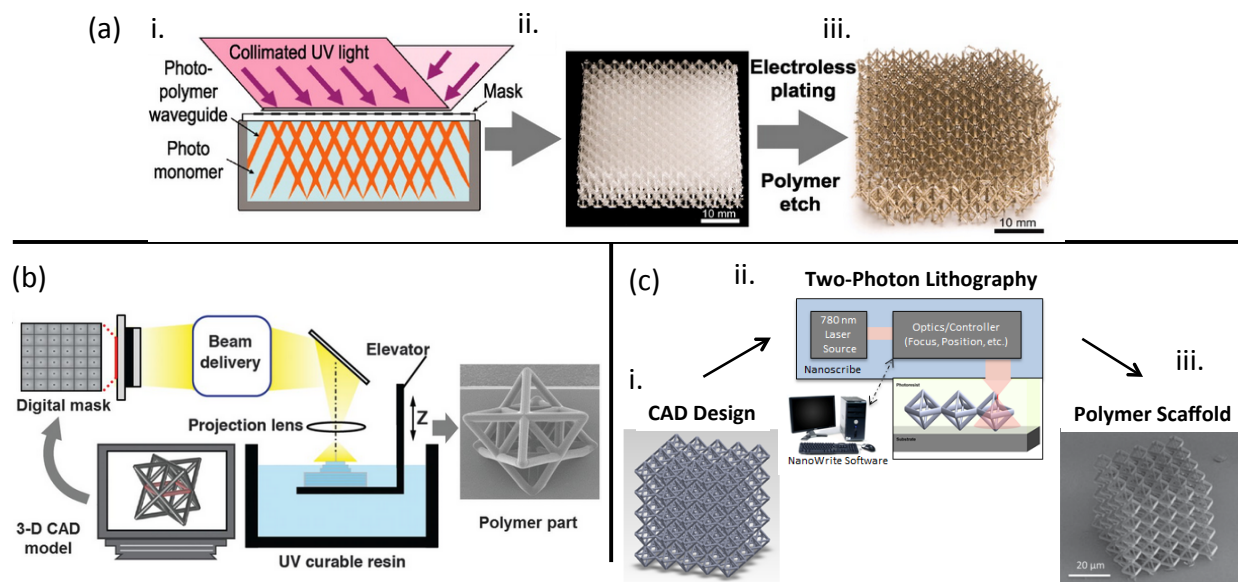


Figure 2: Summary of fabrication methodologies for structural meta-materials.

(a) Three-dimensional array of self-propagating photopolymer waveguides. (i) A photomonomer is exposed to collimated ultraviolet (UV) light through a patterned mask (ii) Polymer templates are electrolessly plated with a conformal thin film, followed by etch removal of the template. (iii) Image of Ni-P microlattice.

Reproduced from²⁹; (b) Projection microstereolithography, a layer-by-layer technique. The substrate is lowered into liquid resin by an elevator traveling vertically; SEM image at the right is the fabricated octet-truss unit cell. Reproduced from³³; (c) Two-photon lithography direct laser writing.

(i) A 3-dimensional structure is designed using CAD software, then (ii) a femtosecond pulsed near-infrared laser is focused into and translated through a UV-curable photoresist leading to two-photon absorption and photopolymerization of the resist in the focal volume. (iii) Samples are placed in a developer solution where unexposed photoresist is washed away, leaving a three-dimensional structure. Reproduced from³⁹

This polymer wave-guide technique is a unique and scalable fabrication method and relies on the difference in the index of refraction between the cross-linked and non-cross-linked polymer^{34,38}. In the subsequent fabrication steps, the polymer scaffold is coated with a thin solid film, such as nickel phosphorus (Ni-P) or metallic glass, and the polymer is removed, leaving behind a fully hollow structure composed of the deposited material^{29,40}. The wave-

guide technique can be used to easily vary the angle and number of bars connecting at a single node and serves as a useful pathway to understanding the relationship between mechanical properties and geometric parameters of ultra-light hollow structures³⁸. This patterning technique is restricted to generating only certain unit cell geometries, which restricts the deformation mode of such architected materials since all geometries deform by bending of the lattice bars under an applied load³⁹. Cellular solids, such as the microlattice, are evaluated using their relative density, or the ratio of the volume contained within a unit cell to the volume of the unit cell, and their mechanical properties, such as strength and stiffness^{22,41}. Classical cellular solids theory relates the strength (σ) and stiffness (E) to relative density ($\bar{\rho}$) as $\sigma \propto \bar{\rho}^n$ and $E \propto \bar{\rho}^m$ ^{22,41}. The exponents, m and n , are determined by the fundamental deformation mechanism of the structure, by either bending or stretching of the lattice struts under an applied load^{21,22}. Bending-dominated structures, such as the microlattice, scale as $m = 2$ and $n = 1.5$; stochastic foams, such as nanoporous Au, have a lower scaling with $m = 3$ and $n = 2$ ^{22,41}; and stretching-dominated structures, such as the octet-truss lattice, scale with $m = n = 1$ ^{22,23,41}. Stretching-dominated geometries are more desired because the strength falls linearly with relative density, in contrast to the more rapid deterioration in bending-dominated structures and in stochastic foams, and this leads to higher strength and stiffness as relative density decreases. The microlattice has a unique structural behavior that emerges as the ratio between strut wall thickness, t , and strut diameter, D , falls below a critical threshold of (t/D) ; this critical ratio is described as $(t/D)_{critical} \sim f(\sigma_{Y,s}, E_s, \theta, \varepsilon_{max})$, where θ is the lattice angle, $\sigma_{Y,s}$ and E_s are the yield stress and strength of the constituent material and ε_{max} is the maximum compressive strain on the microlattice^{40,42}. As the ratio of the wall thickness of the struts to strut diameter falls below

a critical value of $(t/D) < 0.005$ for the Ni microlattices, the lattice completely recovers after strains greater than 50% of the lattice height^{29,40}. The hollow nodes accommodate substantial bending moments, which occur at lower forces than would be required for Euler buckling of the hollow struts, and this is the mechanism responsible for the impressive recovery of the microlattice^{29,40,42,43}.

1.3 Fabrication: Microlattices via Micro-Stereolithography

Similarly-scaled micro-architectures have also been created using micro-stereolithography, shown in **Figure 1b**, which is an additive process where lattices are created in a layer-by-layer fashion similar to that of 3D printing, shown in **Figure 2b**³³. In contrast to the bending-dominated HRL microlattices (**Figures 1c and 2a**), this technique is capable of producing a variety of different geometries, including the octet-truss, which has sufficient nodal connectivity to be a stretching-dominated structure²¹⁻²³. Similar to the coating and etching process of the HRL microlattices, the micro-stereolithography-produced microlattices can also either be made entirely of monolithic polymer struts, or the polymer can serve as a sacrificial scaffold once they are coated with a material, such as Ni-P or alumina (Al_2O_3)³³. Under uniaxial compression, the hollow Ni-P or Al_2O_3 octet-truss microlattices have shown near agreement with the scaling predicted by classical theory, where $\sigma \propto \rho^n$ and $E \propto \rho^m$, with $m = 1.1$ and $n = 1.2 - 2.7$ for relative densities of $\rho = 10^{-4} - 10^{-2}$ ³³. These octet-truss structures outperform the HRL microlattices as predicted by classic cellular solids theory in terms of strength, and this improvement is attributed to a change in characteristic deformation mechanism between bending- and stretching-dominated architectures^{33,29}.

Both types of these hollow microlattices have wall thicknesses in the size regime of where material size effects are observed, but the dimensions of their unit cells are too large to observe or capitalize on the size effects because their deformation behavior can be fully described from the structural point of view, which is independent of material length scales. For example, if the microlattices were scaled up in a self-similar geometry, the mechanisms of deformations would be consistent with those of the microlattices at smaller scales. The microlattices offer many novel properties that result from the interaction of various structural length scales, such as their recovery and energy absorption capabilities; however, it is not appropriate to classify them as meta-materials since their properties can be fully described by classical mechanics theories.

1.4 Fabrication: Nanolattices via Direct Laser Writing Two-Photon Lithography (DLW TPL)

Nanolattices, fabricated by two-photon lithography, enable a size reduction by 3 orders of magnitude from the microlattices described above while still being amenable to the coating and scaffold removal steps. These architected materials have dimensions down to the nanoscale, with typical strut lengths of 3-20 μm , diameters of 150-500nm, and wall thicknesses of 5-600nm^{30,31,39,44,45}. Unlike the microlattices, the individual building blocks that comprise nanolattices are small enough that they cannot be resolved by the human eye; their mechanical properties depend on the combination of the size-dependent material properties and structural response and cannot be predicted solely by scale-free continuum theories³⁰⁻³². These nanolattices were first fabricated out of a specific polymer using a direct laser writing two-photon lithography (DLW TPL) system developed by Nanoscribe GmbH. The two-photon method employs a 780nm femtosecond pulsed laser focused into a

small volume within the polymer, or a voxel, where the two photons released in a single pulse constructively interfere with sufficient energy to cross-link the monomer and harden the material within the voxel. The voxel is elliptically shaped and can be traced in 3-dimensions within a droplet of photoresist to create a polymer structure of any arbitrary geometry, shown in **Figure 2c**^{35,36}. A variety of conventional thin-film deposition techniques lend themselves well to coating these polymer nanolattices^{31,28,39,44,45}. For example, Montemayor, et. al. demonstrated the feasibility of sputtering metals, like Au, onto different types of nanolattices, shown in **Figure 1f**; Meza, et. al. and Bauer, et. al. successfully utilized atomic layer deposition to coat ~5-60nm thick Al₂O₃ and TiN coatings onto the polymer scaffolds, as shown in **Figures 1e** and **1g**, respectively^{31,28,39,44,45}. After deposition, the initial polymer scaffold was exposed by the sides of the sample using a focused ion beam (FIB) and removed using oxygen plasma^{30,31,39,44,45}. The TPL method allows for the angled tubes of a nanolattice to have smooth surfaces in contrast to the rough stair-step edges produced by the layer-by-layer micro-stereolithography method. The wave-guide method produces microlattice with struts that have circular cross-sections, while the nanolattice struts produced by TPL have elliptical cross-sections, with the ellipticity of the tubes decreasing with the unit cell angle, as shown in **Figure 1d**^{30,39,44,45}. Hollow gold nanolattices with octahedron geometry were fabricated, and their response to uniaxial compression as a function of lattice angle and wall thickness revealed that both the strength and stiffness can be increased by an order of magnitude by tuning the geometry for samples of constant relative density, in contrast to the behavior predicted by cellular solids theory, which assumes a constant strength and stiffness for a given relative density^{22,30,41}. The relative density of the nanolattices in the work by Montemayor, et. al. was kept

constant at $\bar{\rho} = 0.05$ by varying the unit cell size, from 5-20 μm , and strut wall thickness from 200-661nm³⁰. The lattice angle of the octahedron unit cell was increased from 30° to 60°, for a fixed wall thickness of $\sim 300\text{nm}$, and an increase of approximately an order of magnitude was observed in both the strength and stiffness in these bending-dominated cellular solids³⁰. To examine the effect of material size effects on the 45° octahedron nanolattices, the wall thickness was varied from $\sim 200\text{-}635\text{nm}$ and an increase of 150% in strength was observed while the modulus remained unchanged³⁰. According to the classic theory for cellular solids, these nanolattices should all have a fixed strength and stiffness, since both strength and stiffness are only functions of relative density and the deformation mechanism of the lattice³⁰. This study demonstrates that both structural and material size effects can be exploited and tuned independently to elicit novel mechanical properties that would not exist in a larger version of a self-similar structure³⁰.

Hollow alumina (Al_2O_3) nanolattices of the octet-truss geometry with relative densities ranging from $\rho = 10^{-4}$ - 10^{-1} were fabricated with the lattice unit cell dimensions ranging from 5 - 15 μm and the wall thickness of the Al_2O_3 coating ranging from 5 - 60nm³¹. These nanolattices scaled with relative density as $\sigma \propto \rho^n$ and $E \propto \rho^m$ with $m = 1.76$ and $n = 1.61$; the expected scaling of such a stretching-dominated structure should be $m = n = 1$ ^{22,23,31}. This discrepancy between theory and experiments has also been corroborated through finite element computations and the models attribute the greater exponent to the presence of the hollow nodes, which act as a series of discrete instability points within the lattice, and lead to bending-dominated-like deformation initiating at the hollow nodes despite stretching-dominated architecture^{29,43}. The effect of the hollow nodes on deformation and strength of nanolattices cannot be underestimated and remains to be fully

understood. The Al_2O_3 nanolattices undergo significant recovery, of up to 98% of their initial height after uniaxial compressions in excess of 50%³¹. Their ductile-like deformation and recoverability has been attributed to the critical ratio between the wall thickness (t) and the semi-major axis (a) of the hollow elliptical strut cross-section. When (t/a) is below the critical value of ~ 0.03 , the nanolattices exhibit shell buckling behavior and recover after deformation; at greater (t/a) the nanolattices fail catastrophically with little to no recovery³¹. The constituent Al_2O_3 is brittle but as the wall thickness decreases to the nm regime, the Al_2O_3 statistically contains fewer flaws, according to a Weibull distribution, and a material size effect emerges, in addition to the structural effect of the (t/a) ratio; these two effects work in concert to produce the unique material properties of the Al_2O_3 nanolattices^{31,44}. Bauer, et. al. also studied non-hollow Al_2O_3 coated polymer nanolattices fabricated using the DLW TPL method²⁸. Lattices with varying degrees of triangulated bracing, from octet-truss to non-rigid cubic lattices, as well as honeycomb-like structures, both with rigid and non-rigid walls, were subject to uniaxial compression and exhibited significant increases in strength as the Al_2O_3 coating thickness increased²⁸. The Al_2O_3 coating thickness varied from 10 - 200nm, and their density spanned from 100-1000 kg/m^3 ²⁸. For the fully triangulated composite octet-truss lattices, the failure strength increased over an order of magnitude, from $\sim 2 - 35$ MPa, as the thickness of coated Al_2O_3 ranged from 0-200nm²⁸. The modulus also increased from 77 MPa to 1.5GPa, over the same increase in Al_2O_3 thickness²⁸. As the thickness of the Al_2O_3 coating increases, the structures exhibit a transition from buckling to catastrophic fracture and failure of the lattice struts occurs either at the nodes or along the struts²⁸. For all structures that fail by fracture, the thinner Al_2O_3 coatings in the composite structures carry higher tensile

stresses than their thicker counterparts prior to failure; this behavior is attributed to the emergence of the nanoscale flaw tolerance as the thickness of the Al₂O₃ coating is decreased²⁸. For the thinnest Al₂O₃ coatings of 10nm in the composite nanolattices, micro cracks and localized fracture were observed along the strut lengths and the samples did not fail by fracture of the struts or nodes²⁸. The optimized honeycomb lattice composites, with rigid walls, outperformed the existing engineering foams with comparable relative density of 1000 kg/m³ by almost an order of magnitude, at compressive strengths of 280 MPa for the 50nm Al₂O₃ case²⁸. Both the hollow and composite Al₂O₃ nanolattices reach new material property space in terms of strength and stiffness, for their given relative densities, while eliciting many novel properties of brittle architected materials that result from both material and structural effects^{31,28}.

The interplay of structural and material size effects has also been observed in structures with solid metal struts as the constituent building blocks of the lattice and are created using a similar method to the hollow nanolattices³². Copper meso-lattices, shown in **Figure 1h**, were created using an inverse DLW TPL method to first create a negative of the lattice by patterning in a positive-tone resist and electroplating the metal into the exposed pores³². The polymer mold was subsequently removed to reveal a meso-lattice with solid nodes and struts, with diameters on the order of 2 μ m³². The average grain size for electrochemically deposited Cu was 2 μ m, which enabled it to span the entire strut diameter. These meso-lattices had relative densities ranging from $\rho = 0.4 - 0.8$, with the unit cell sizes of 6 μ m and 8 μ m, and had compressive yield strengths of 330MPa, which is up to 80% higher than that of bulk Cu, at 133MPa³². For relative densities of $\rho = 0.8$, strengths of ~ 330 MPa were observed and this is attributed to the emergence of *smaller is stronger*

material size effect that emerges in the micron sized struts³². The meso-lattice with architected small scale Cu struts outperform bulk Cu for relative densities of $\rho > 0.6$, or when up to 40% of the material is removed from a monolithic cube, by a factor of up to 2.5. This means that by introducing architecture, it is possible to significantly reduce the weight of the material while simultaneously strengthening it, a finding diametrically opposite of what is predicted by classical theories³². The rule of mixtures can be used to predict an upper limit for the yield strength of the higher density meso-lattices while classical cellular solids scaling predictions for the octet-truss provide a lower limit for the yield stress of the meso-lattice for relative densities of 0.3; this agreement for low relative densities is expected based on the underlying assumptions of the classical cellular solids theory^{32,41}. In contrast to the microlattices, if the nano- and meso-lattices were scaled up in a self-similar fashion, no unique mechanical properties would emerge because once the smallest external dimension is increased above a few microns, the coupling between structural and material properties that is present at the nano-scale would vanish. This is one of the main reasons why the meso- and nanolattices can also be described as novel structural meta-materials.

This chapter highlights the state of the art on structural meta-materials with dimensions on the order of microns down to nanometers and the mechanical properties are summarized for comparison in **Table 1** (Data compiled from references^{28-31,33,44-46}). Small-scale lattice structures have demonstrated that unique material size effects can effectively be proliferated to larger structures and as a result, there is potential to create new classes of bulk engineering materials with properties that don't currently exist³⁰⁻³². Utilizing architectural features as key elements in defining multi-dimensional material

design space promises to enable independent manipulation of the currently coupled physical attributes and to develop materials with unprecedented capabilities.

Lattice Type	Fabrication Method	Lattice Material	Wall Thickness (nm)	Relative Density ρ	Strength σ (MPa)	Young's Modulus E (kPa)
Microlattice (Bending-, Stretching-dominated)	Polymer waveguide, micro-stereolithography	Polymer, Hollow Ni, Hollow NiP, Hollow/Solid Al_2O_3	40-210 Al_2O_3 100-1000 NiP 100-500 Ni	$10^{-4} - 10^{-2}$	0.009 – 2.9	$10^{-1} - 10^8$
Nanolattice (Bending-, Stretching-dominated)	DLW TPL	Polymer, Au, Al_2O_3 , Polymer/ Al_2O_3 composite	200-700nm Au 5-60nm Al_2O_3	$10^{-3} - 10^{-1}$	$10^{-1} - 10^2$	$1 - 10^3$
Meso-lattice (Stretching-dominated)	DLW TPL	Cu	-	0.4 – 0.8	50 - 350	-

Table 1: Summary of structural meta-materials in terms of fabrication method, relative density, strength, and modulus.

Using architectural features to elicit desired functionality will shift the material creation paradigm from structure driving processing and material properties to the desired material property driving the architecture and thus the fabrication method. Feasibility of this “reverse” material construction approach, is gated by our ability *to understand* and *predict* mechanical response of these meta-materials, or materials whose properties are controlled by their engineered structure rather than by atomic composition alone, where a new design parameter, *feature size*, plays a critical role. The research in the field of architected meta-materials has profound implications not only for understanding the fundamental physics of the unique effects that emerge in nano-materials but also for

proliferating these so-called size effects into the design of real materials. This approach could fundamentally shift the way people think about the creation of materials, with the concept of the reverse design of materials shifting the paradigm of material creation away from relying on classical processing routes, which are notorious for coupling properties like strength and density; with strong materials also usually being very dense and heavy. The methodologies and work presented in this thesis demonstrate the ability of nanolattices to serve as tunable, in terms of stiffness and strength, and flaw tolerant materials.

Chapter 2: Design and Fabrication of Hollow Rigid Nanolattices Via Two-Photon Lithography

Adapted from:

Montemayor, L. C., Meza, L. R. & Greer, J. R. "Design and Fabrication of Hollow Rigid Nanolattices via Two-Photon Lithography". *Adv. Eng. Mater.* **16**, 184–189 (2014).

2.1 Fabrication of Polymer Nanolattices via TPL DLW

This chapter describes the fabrication of hollow metallic nanolattices with dimensions spanning from 100nm to 1 μ m to 10 μ m and larger. The two-photon lithography fabrication process shown in **Figure 3** was used to create the 3-dimensional structures that were designed using SolidWorks, a computer aided design (CAD) program, as shown in Figure 3a.

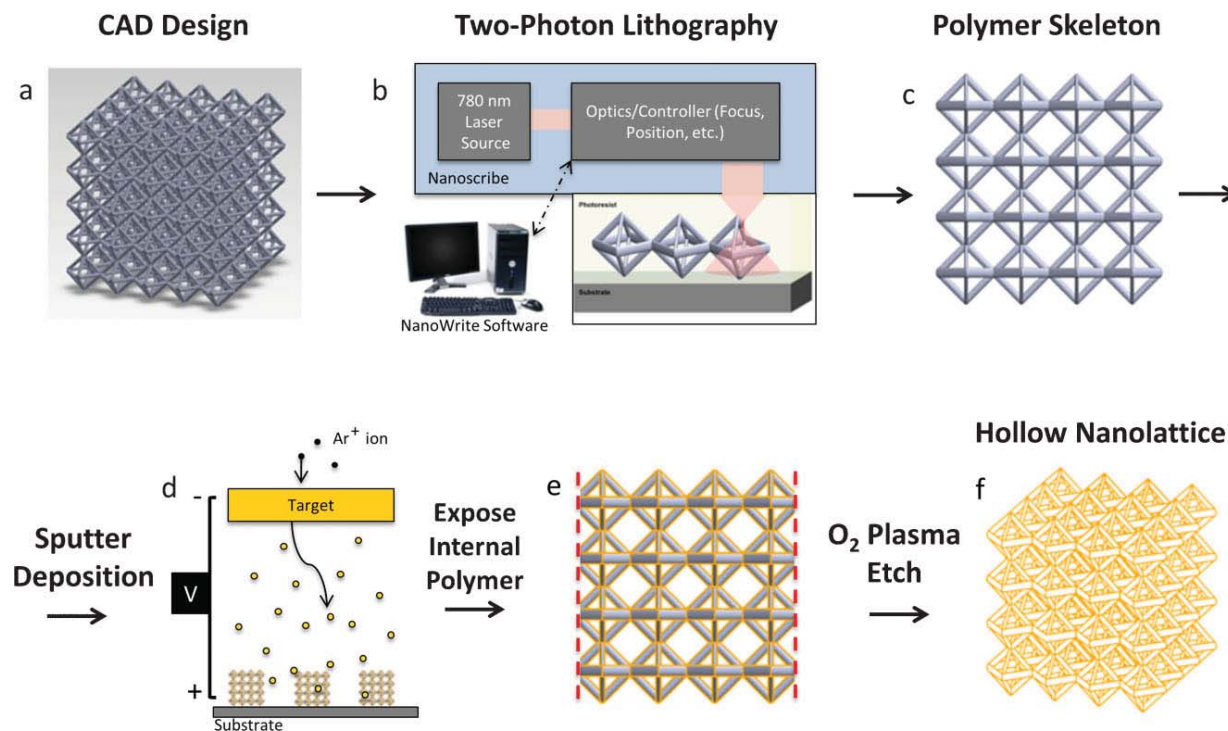


Figure 3: Fabrication process to create hollow rigid nanolattices.

A 3-dimensional structure is designed using CAD software (a) and then replicated into a polymer pattern using two-photon lithography (b). After development, the polymer structure (c) is conformally coated with a thin metallic layer via sputtering (d). The edges are removed using a focused ion beam to uncap polymer within each strut (e), and the entire polymer skeleton is removed using an oxygen plasma etch, revealing a hollow, rigid nanolattice (f).

The design was then imported as a set of points describing the vertices of the unit cell, which defines the structure, to NanoWrite, a program that interfaces with the Nanoscribe TPL instrument to write the designed structure in a polymer. The unit cell was then patterned to create nanolattice arrays that were 5 x 5 x 3-5 unit cells large, depending on the geometry, to make structures with dimensions of approximately 50 μ m x 50 μ m x 50 μ m. Once the structure was defined and imported into the NanoWrite Software, the IP-Dip photoresist, specially design by Nanoscribe GmbH to optimize the TPL process, was exposed to a 780nm femtosecond pulsed laser. The laser was focused to a region denoted as the voxel, which is elliptically shaped with an aspect ratio of 2.5 and has sufficient

energy to initiate cross-linking of the photoresist to create the polymer structure.^[21] The voxel was traced in 3 dimensions according to the points defining the structure by a piezoelectric motor, with a resolution of $\pm 10\text{nm}$ and a maximum displacement of $300\mu\text{m}$. By altering the power of the laser and the speed with which the voxel moves through the photoresist, the size of the voxel and the exposure of the photoresist can be controlled to create features as small as 150 nm .^[19, 20]

A parameter matrix varying the laser power and writing speed was explored to determine the optimal parameters for creating structurally stable arrays. When the laser power/write speeds were too low, the structures collapsed under capillary forces during the development process. On the opposite end of the spectrum, when the laser power/write speeds were too high, certain regions within the photoresist experienced very high-energy concentrations, which led to small-scale explosions and destroyed the structures (See Appendix A). The laser power was varied from $8 - 12\text{mW}$ in increments of approximately 0.67 mW and the writing speed varied from $45 - 70\ \mu\text{m/s}$ in increments of $4.17\ \mu\text{m/s}$ for the octet structure. This produced an exposure matrix covering 6 laser powers and 6 write speeds, for a total of 36 different exposures. The best structures were produced for photoresist exposure with speeds between $45\text{-}50\ \mu\text{m/s}$ and laser powers of $8.8\text{-}11.2\ \text{mW}$ and the optimal conditions were chosen to be at $45\ \mu\text{m/s}$ and 10mW for the structures shown in this work. After exposing the photoresist, the structures were developed for 30 minutes in propylene glycol mono-methyl ether acetate (PGMEA) followed by a 3-minute rinse in isopropyl alcohol.

2.2 Conformal Sputtering of Nanolattices

Once the polymer nanolattice was isolated, it was then coated using sputter deposition, as shown in **Figure 3 c-d**. To demonstrate the fabrication process, gold was used to sputter coat the polymer nanolattices. The conformality of the gold coating depends on the pressure, power, and deposition time during the sputtering process. Various pressures, powers, and times were investigated to determine the optimal sputtering parameters. Gold was chosen as the model sputtering material primarily because it does not react with the oxygen plasma required to remove the polymer at a later step in the fabrication process, though it is a representative material and any material resistant to oxygen plasma that can be sputtered can be used for this fabrication process. A DC power source was used for the sputtering process and initial parameters of 100 W and a working pressure of 3mTorr with argon at 10 sccm was tested. For a 30-minute deposition time, the structures did not coat conformally so the time was increased to 60 minutes. After 60 minutes of gold deposition at these parameters, the structures appeared to have a more conformal coating. To improve the coating, powers of 100 and 50W and pressures of 3 and 5 mTorr were tried, resulting in a total of 4 sputtering conditions, keeping the sputtering time constant at 60 minutes and the carrier gas as argon at 10 sccm. For conditions of 100W and 5mTorr, the coating was very flaky and did not adhere well to the structure or substrate. The most conformal coating for the octet, octahedron, and kagome structures was found to be at 50W and 5mTorr. As shown in **Figure 3 e-f**, the remaining structure after the FIB/etch process described above is a hollow, rigid nanolattice. For gold, the optimal parameters were found to be at a working pressure of 5mTorr and a power of 50W for a carrier gas of argon flowing at 10sccm.

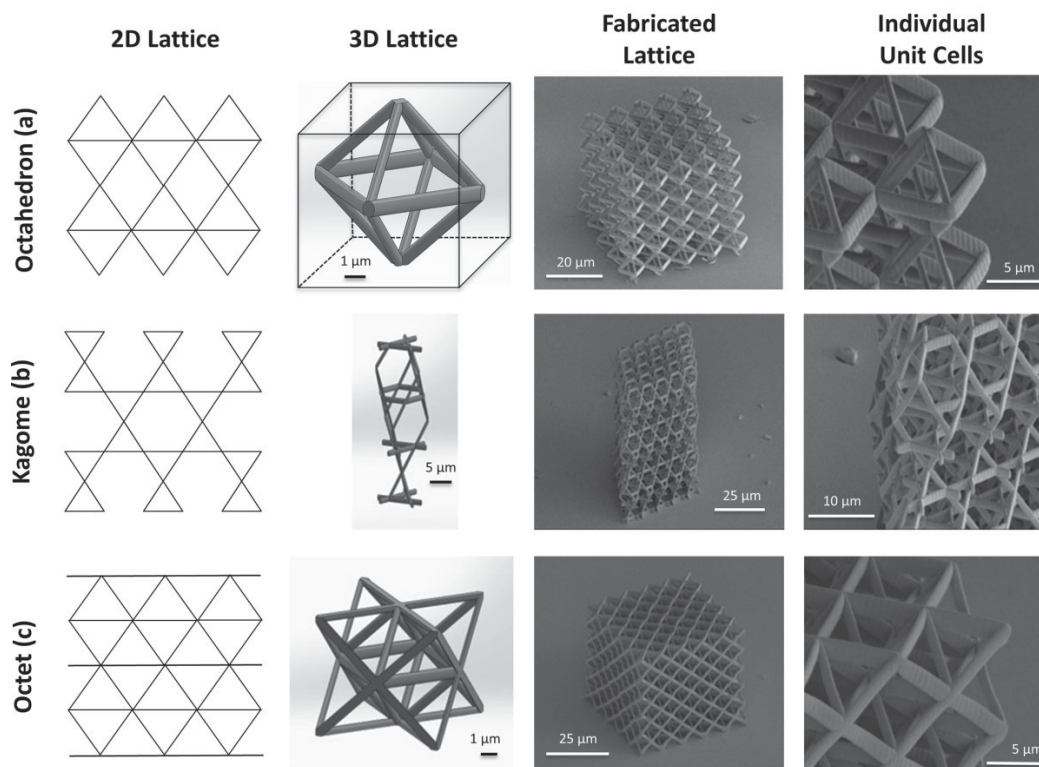


Figure 4: CAD model and SEM images of fabricated structures for three different nanolattice geometries. Octahedron (a), kagome (b), and octet (c). The fabricated structures closely match the design at each relevant scale. The 3D octahedron (a) demonstrates the volumes used to calculate relative density, as detailed in the Section 1 (image tilt of 55°–60°).

The gold was sputtered for 60 minutes under these conditions resulting in a gold layer of approximately 90nm on the nanolattice surface. As shown in **Figure 4**, the fabricated structures after sputtering deposition closely matched the computer designed structures on all relevant length scales for three different nanolattice geometries.

2.3 O₂ Plasma Etching to Create Hollow Nanolattices

After the polymer lattices were coated in gold, this initial scaffold was removed to reveal hollow metallic nanolattices. To remove the polymer, the structure was exposed to an oxygen plasma treatment at a pressure of 1 Torr and flow of 300 sccm O₂ for 2 hours.

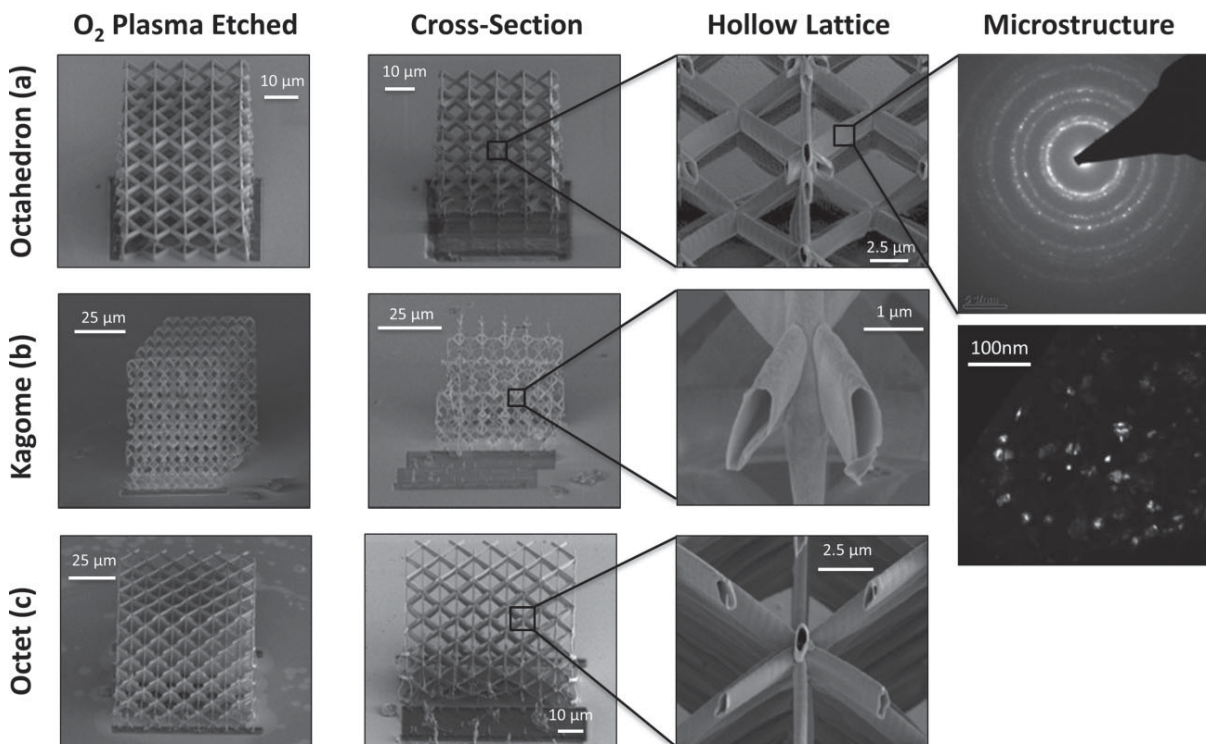


Figure 5: SEM images of the hollow structures for the three lattice geometries. Octahedron (a), kagome (b), and octet (c) after sputtering and etching steps as shown in Figure 3 (image tilt of 52°). Representative transmission electron microscopy (TEM) dark-field image of an octahedron lattice member showing the nanocrystalline structure of the sputtered coating with grain size on the order of 20–50 nm.

The nanolattices were milled on 2 sides with a focused ion beam (FIB) at a current density of 7 nA to expose the polymer so the oxygen plasma could penetrate inside the scaffold and etch away the polymer. After the process shown in **Figure 3**, the fabricated structures were sliced 1/3, 1/2, and/or 2/3 along the depth of the lattice using the FIB, with the conditions described above, and then visually inspected to assess the conformality of the gold coating. **Figure 5** shows representative cuts through various types of structures and verifies the conformality of the coating through the depth of the nanolattice. By analyzing the cross-sectional thickness of the hollow nanolattice members, it was verified that the approximate thickness of the gold coating, under the optimal sputtering conditions described above, was 90 ± 30 nm. The coating thickness was averaged over 20–50 thickness measurements at

various lattice depths and locations for each of the octahedron, kagome, and octet nanolattice geometries.

2.4 Calculating Relative Density of Hollow Nanolattices

In addition to the sputtering conditions, the relative density of the polymer structure plays a role in the degree of metallic film uniformity. A solid rather than a hollow nanolattice was used to calculate the relative density because it is the diffusion of the sputtered material into the polymer structure that creates a conformal coating on the nanolattice. The relative density of a nanolattice depends both on the geometry and size of the unit cell. The relative density of the structures was calculated by considering the volume fraction of the structure, which is equivalent to the density of the cellular structure over the bulk density for a given material^{22,41}. The conformality of the coating depended on the relative density of the structure on which is being coated. In this case, the relative density of the solid member polymer structure is the density that must be considered. To calculate the volume of the polymer structure, a SolidWorks model of the unit cell was used. Dimensions of the structure in SolidWorks were set using the measured dimensions of the polymer structured based on SEM images. Using these dimensions, the volume of the polymer unit cell contained in the unit cell was calculated using the SolidWorks model. The volume fraction was found by dividing the volume of the polymer structure contained in the unit cell by the volume of the unit cell, demonstrated in **Figure 4a** for the octahedron structure, which is equivalent to the relative density of the structure. A single unit cell was considered in this calculation since the volume of the structure and the bulk both scale by the number of units cells that form the lattice. The calculated relative densities for the

various geometries are shown in **Figure 6**. Both the octahedron and octet unit cells can be contained in a $10\mu\text{m} \times 10\mu\text{m} \times 10\mu\text{m}$ unit cell volume since the angle between non-perpendicular members is defined to be 45 degrees. For a unit cell volume of $10\mu\text{m} \times 10\mu\text{m} \times 10\mu\text{m}$, the octahedron has a relative density of 0.025 and the octet structure has a higher relative density of 0.049 due to additional members in the unit cell. **Figure 6** shows that the sputtering process did not coat the octet nanolattice conformally at relative densities higher than approximately 0.025. When the unit cell dimensions of the octet structure increased from $10\mu\text{m} \times 10\mu\text{m} \times 10\mu\text{m}$ to $15\mu\text{m} \times 15\mu\text{m} \times 15\mu\text{m}$, the relative density became 0.022 and the structure could be conformally coated with the sputtering conditions described above.

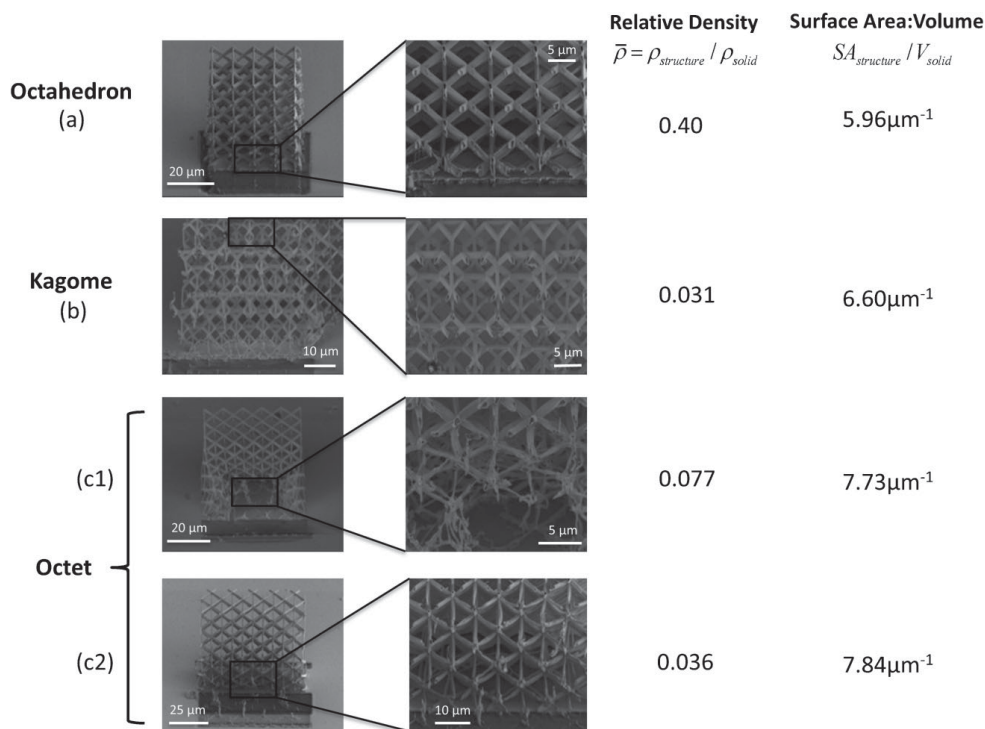


Figure 6: SEM images of representative nanolattices for different relative densities and geometries.. For relative densities of $\bar{\rho} \sim 0.040$, the octahedron (a), kagome (b), and octet (c2) structures coat conformally under optimal sputtering conditions. For higher relative densities, such as octet (c1), the sputtering is not conformal throughout the structure. Note the high surface area to volume ratio for each of the nanolattice structures, making these structures ideal for solar/fuel cell applications.

For a kagome lattice with a similar relative density of 0.024, the gold coating was also found to be conformal. **Figure 6** shows three lattice geometries that can be coated conformally using sputter deposition, though for structures with relative densities higher than approximately 0.025, the coating began to lose integrity.

2.5 Conclusions

This chapter demonstrates a methodology to create 3-dimensional hollow metallic hierarchical structures with length scales spanning from hundreds of nanometers generated to 50 microns using a two-photon lithography technique. The ability to fabricate structures not limited by geometry with higher resolution than previous technologies provides an opportunity to engineer structures at many length scales. Ultra-lightweight, low density structures can now be engineered and fabricated with this methodology to outperform those that currently exist, such as stochastic foams, by controlling the lattice geometry. Not only can the deformation mechanism of the structure on the macro-scale be controlled through the geometry, thus potentially improving its material properties, but the hierarchical nature also provides opportunities to harness the “smaller is stronger” size effect that has been observed in metals on the nanoscale.^[22, 23] This size effect has previously been observed in nano-pillars but the ability to potentially harness this effect in a more structurally robust system allows for the size effect to be utilized in a variety of applications. The fabrication process demonstrated in this chapter presents a way to create a structure with potential to capitalize on the combined effects of lattice geometry and size-induced material properties with potential applications ranging from biocompatible structural materials to fuel and solar cells.

Chapter 3: Mechanical Response of Hollow Metallic Nanolattices: Combining Structural and Material Size Effects

Adapted from:

Montemayor, L. C. & Greer, J. R. "Mechanical Response of Hollow Metallic Nanolattices: Combining Structural and Material Size Effects". *J. Appl. Mech.*, doi: 10.1115/1.40303061 (2015).

3.1 Introduction

The mechanical performance of such architected solids on the macro-scale is a function of the deformation mechanism and relative density of the structure, as well as of the constituent material properties, and this has been studied for both materials with cellular solid cores as well as bulk cellular solids^{17-20,22,23,33,29,31,40,41,43,44,47-49}. Cellular solids can deform by either bending or stretching of the elements, which is dictated by the geometry of the lattice and its nodal connectivity, and this bending or stretching behavior defines the deformation mechanism of the cellular solid^{21-24,41}. A 3-dimensional structure must have a connectivity of $Z = 6$ at the nodes to be rigid and a connectivity of $Z = 12$ to be stretching-dominated; structures with $6 \leq Z < 12$ are bending-dominated²¹. The structural deformation mechanism, determined by the nodal connectivity, directly impacts the modulus and yield strength of the overall structure^{22,41}. The modulus and yield strength are also related to the structure's relative density, $\bar{\rho}$, which is defined as the volume of the lattice contained within a unit cell divided by the volume of the unit cell⁴¹. The yield

strength and modulus of 3D open-cell *bending-dominated* structures, such as honeycombs or octahedron lattices, scale as $\sigma_y = 0.3\bar{\rho}^{1.5}\sigma_{ys}$ and $E = \bar{\rho}^2 E_s$, where σ_{ys} and E_s are the yield strength and modulus of the constituent material ^{22,41}. For 3D *stretching-dominated* structures, such as the octet-truss lattice, the yield strength and modulus scale as $\sigma_y = 0.3\bar{\rho}\sigma_{ys}$ and $E = 0.3\bar{\rho}E_s$, which causes strength to decrease less rapidly than that of bending-dominated structures as relative density decreases ^{22,23}.

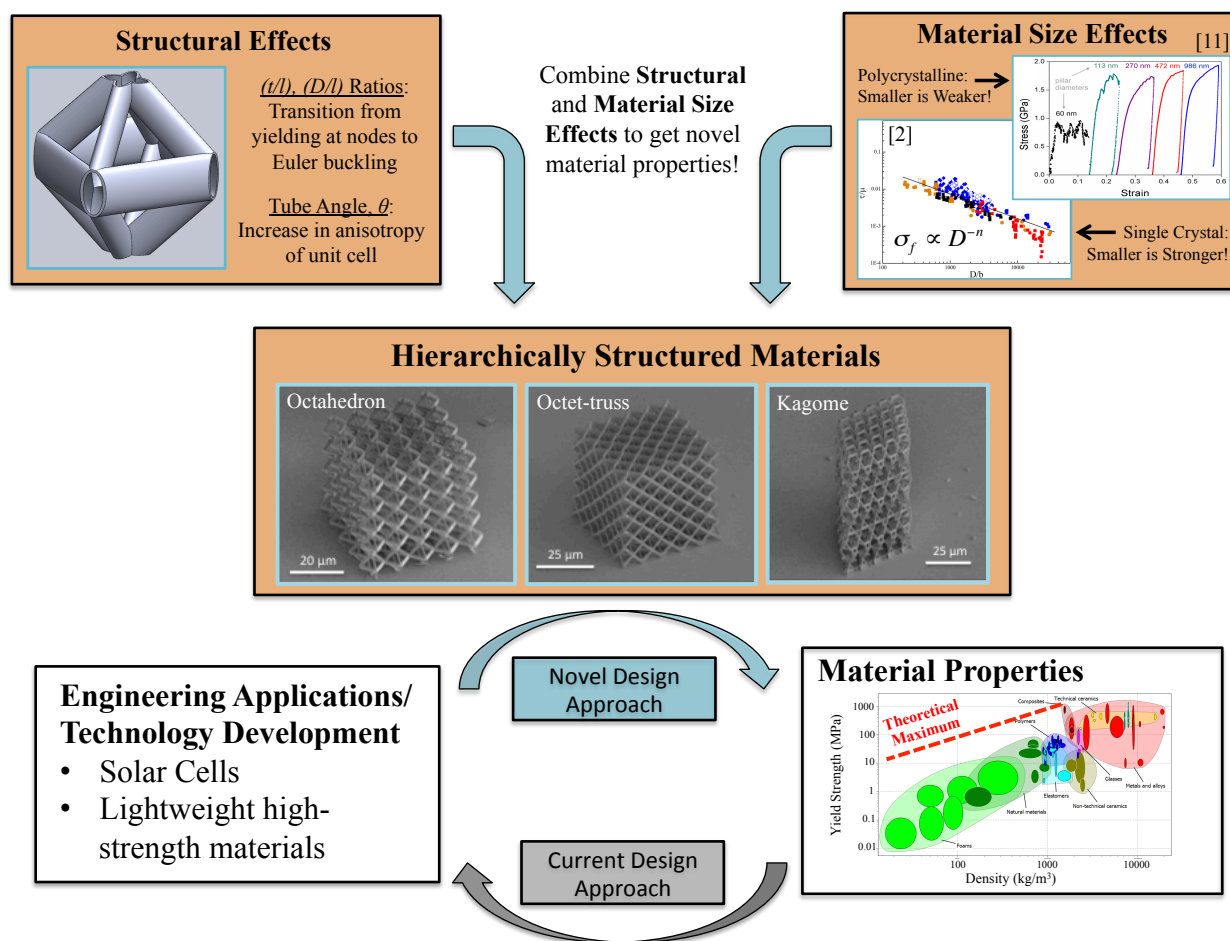


Figure 7: Hierarchically structured materials combine structural and material size effects to enhance material properties and provide opportunities to create new materials that outperform existing materials. [Material properties chart generated using CES Selector (image courtesy of S. Das). Figures reprinted with permission from references^{2,11}.]

A theoretical upper limit for strength and modulus of cellular solids exists as a function of relative density because the mechanical properties of the lattice depend on the constituent material properties. All existing engineering materials with densities lower than 100 kg/m^3 fall below this theoretical maximum by an order of magnitude or more, leaving a prominent “white space” in the strength vs. density material property space, shown in **Figure 7**²². When calculating this material property space, the strength and stiffness of the constituent materials are assumed to be constant so the deformation mechanism of the structure represents the only variable parameter. For macroscale cellular solids, this assumption is reasonable because yield strength is independent of size for materials at this length scale. Below the micron scale, many different classes of materials exhibit size effects, such as “*smaller is stronger*” in single crystalline metals¹⁻⁵, “*smaller is weaker*” in nanocrystalline metals^{2,6,10-12}, and “*smaller is ductile*” in metallic glasses and ceramics^{2,13-16}. This renders the mechanical properties of materials at these dimensions different from bulk, and these properties are no longer constant. Creating hierarchical structural geometries with sub-micron dimensions, such as nanolattices, has been shown to provide a pathway to control and tune the strength and stiffness of cellular solids.

3.2 Background: Cellular Solids

Relative densities of cellular solids can be modulated by several approaches, for example, by using hollow tubes instead of solid rods within the same architecture. When hollow tubes are utilized in low-density cellular solids, structural effects can be activated by changes in the various ratios of geometric parameters that define the lattice tubes. While these structural effects do not fundamentally change the deformation mechanism of

the entire lattice, deformation in the individual lattice tubes can be tuned by changing the geometry. For example, the compressive response of hollow thin-walled Ni-based microlattices demonstrated that its deformation behavior and recoverability depend on the geometric parameters of the lattice tubes, like the tube diameter-to-length ratio, D/l , and wall thickness-to-diameter ratio, t/l ^{13,29,40,42,43,50,51}. Valdevit, et. al proposed a model in which the deformation mechanism of the individual microlattice tubes transitions from Euler buckling to yielding of the constituent material at the nodes at a critical relative density, which is directly proportional to (D/l) and (t/l) ⁴³. This model assumes that all members of the unit cell carry equal force and that the maximum bending moment occurs at the nodes; the stress at the node is not taken into account ⁴³. The results of this analytic model compared favorably with those of the finite element simulations (FEM) that account for the complex nodal geometry, where the latter also exhibited a critical relative density at which the deformation mode of the tubes transitioned from Euler buckling to yielding, albeit at lower overall stresses, and the transition occurred at a lower relative density ⁴³. Torrents et. al. proposed a simple analytic model that predicts a critical (t/D) ratio above which plastic deformation begins. This critical $(t/D)_{crit}$ is a function of the constituent material properties, tube angle, and maximum global strain of the microlattice ⁴⁰. Compression experiments showed that the microlattices fully recovered after 50% compressive strain for $(t/D) < (t/D)_{crit}$, which has been demonstrated for a variety of materials ^{40,42}. While the geometric ratios of the microlattices impact the deformation mechanism of the individual tubes, macroscopic parameters of the overall lattice, such as the lattice angle, also affect the mechanical response of the structure. Previous work

defined the lattice angle to be the angle between the horizontal mid-plane of the unit cell and the lattice tubes, as shown in **Figure 8**^{34,38}.

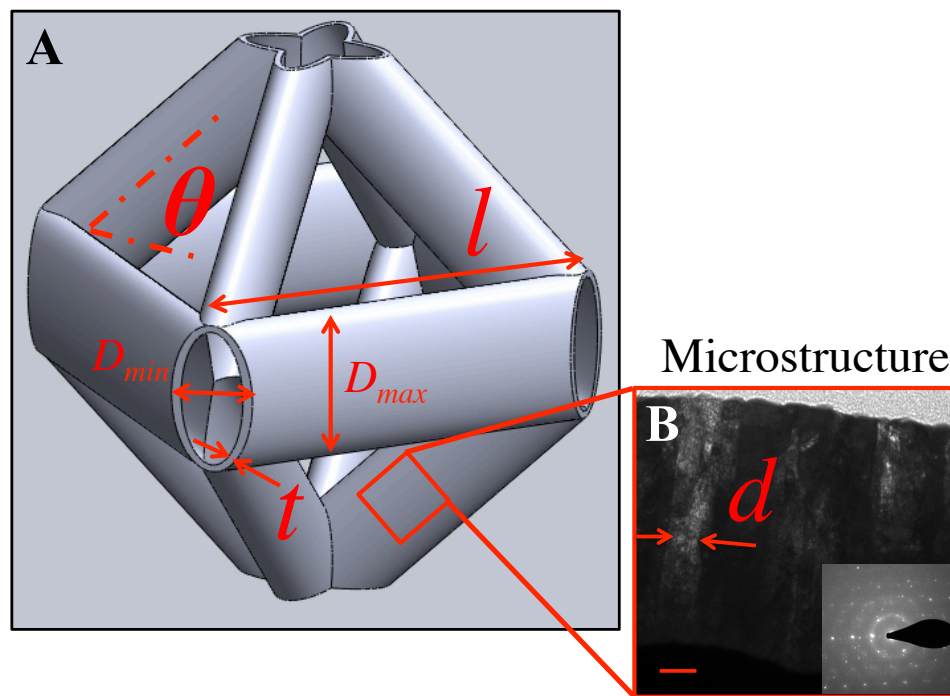


Figure 8: Schematic of relevant geometric parameters on a nanolattice unit cell (A) and TEM image showing columnar grain structure of tubes with grain size on the order of 50nm (B). (TEM courtesy of Z. Aitken, scale bar 100nm)

Jacobsen, et. al. showed that strength and stiffness of solid polymer microlattices increased with higher lattice angle, as predicted by classical mechanics³⁴. The calculated stiffness of the microlattices was found to be within 15% of the model proposed by Deshpande et. al., which predicts that for a pyramidal core (stretching-dominated), the stiffness scales as $E = E_s \bar{\rho} (\sin \theta)^4$ ^{20,34}. The microlattices presented in the work by Jacobsen, et. al. have a connectivity of $Z = 8$, which does not rigorously satisfy the condition for a stretching-dominated structure and might explain the observed discrepancy between the model and the experiments³⁴. Previous work on microlattices demonstrates the

importance of understanding structural effects that may potentially couple with material size effects in complex hollow tube architectures and provides insight to utilizing structural effects in 3-dimensional architected materials^{13,20,29,34,40,42,43,50,51}. Valdevit, et. al have shown in simulation that the analytical predictions for strength and stiffness where $\sigma_y \propto \bar{\rho}^m$ and $E \propto \bar{\rho}^n$ over predict the strength of a hollow cellular solid by as much as an order of magnitude and the experimental results on hollow microlattices agree with the finite element simulations for a periodic cellular solid with hollow nodes^{41,43}. Torrents, et. al have shown for the microlattices that the strength follows the analytically predicted scaling relations; however, again a knock-down in strength is observed and this is attributed to the complex stress state at the hollow nodes under uniaxial loading⁴⁰. Recently, Zheng, et. al demonstrated the ability to create ceramic and ceramic-polymer composite structures with multiple geometries, on the same length scales as the microlattices, using a micro-stereolithographic process³³. For stretching-dominated structures in the work by Zheng, et. al, the strength was found to scale as $\sigma_y \propto \bar{\rho}$ and the modulus as $E \propto \bar{\rho}$, for $10^{-4} < \bar{\rho} < 10^{-1}$, which agrees with the classical theory proposed by Gibson and Ashby for stretching-dominated cellular solids^{33,41}. Meza et. al have proposed a model to describe the local deformation behavior of the nanolattices by considering the compression of a single half unit cell; they found that the deformation of the tubes was governed by lateral torsional bending, which is caused by minor geometric imperfections at the nodes and these results agree with the experimental data^{44,45}. Meza, et. al have also reported the mechanical behavior of stretching-dominated alumina nanolattices that were fabricated using two-photon lithography followed by deposition of a rigid coating and etching out of the polymer scaffold and found that the strength scales as $\sigma_y \propto \bar{\rho}^{1.76}$, the

modulus scales as $E \propto \bar{\rho}^{-1.61}$, and that the structures recovered after compression in excess of 50% ³¹. The decrease in scaling for both strength and stiffness is attributed primarily to the complex stress state at the hollow nodes and the minor geometric imperfections of the nanolattices ³¹.

3.3 Background: Material Size Effects

3.3.1 Uniaxial Deformation

A variety of material size effects have been observed in nanoscale samples with different microstructures ^{1-6,10-12}. Single crystalline nanopillars exhibit a “*smaller is stronger*” size effect demonstrated through experiments, theory, and computations for face-centered (FCC), body-centered cubic (BCC), hexagonal close-packed (HCP) metals ¹⁻⁹. For example, the yield strength of single crystalline face-centered cubic (FCC) metals can be described by a power law dependence between strength and size, $\sigma \propto D^{-n}$, where D is the pillar diameter and n ranges between 0.5 and 0.7 ^{1,2,5,6}. Nanocrystalline metals with similar external dimensions exhibit the opposite effect on strength, with the emergence of a “*smaller is weaker*” size effect at a critical sample size-to-grain size ratio, (D/d) , unique to each material. For example, Pt nanopillars with 12nm grains had a critical (D/d) of 5-10; in Ni nanopillars with 60nm grains, the weakening occurred for (D/d) between 15-30, and in polycrystalline Cu samples weakening was observed in experiments and simulations for $(D/d) < 10$ ¹⁰⁻¹². Gu et. al. proposed a model that describes how the yield strength of a nanocrystalline metal changes as a function of the diameter of a cylindrical sample relative to the material grain size ¹¹. This model assumes that only the grains in the outer shell interact with the free surface and the grains in the inner core of the sample are not affected by it ¹¹. The model predicts that for large D/d , the strength approaches the bulk strength,

and for small D/d , the deformation is dominated by grain boundary sliding, which weakens the sample ¹¹. **Equation 1** shows the relationship between the yield strength and the sample size-to-grain size ratio, where d is the grain size, D is the sample size, σ_Y^s is the stress required to initiate grain boundary sliding, and $\sigma_{y(bulk)}$ is the strength of the bulk material with the same microstructure ¹¹.

$$\frac{\sigma_{n(Au)}}{\sigma_{y(bulk)}} = \left(1 - \frac{d}{D}\right)^2 + \frac{\sigma_Y^s}{\sigma_{y(bulk)}} \left[1 - \left(1 - \frac{d}{D}\right)^2\right] \quad \text{Eqn. (1)}$$

3.3.2 Beyond Nano-pillars: Deformation under Complex Stress States

Hierarchical architected structures allow opportunities for material size effects to be utilized because the novel material properties present at the sub-micron length scales can be proliferated onto a larger structure. Hodge et. al. showed that a stochastic nanocrystalline Au nanoporous open-cell foam exhibits a “*smaller is stronger*” size effect as the ligament size decreases from 900nm to 10nm; these foams outperform the expected strength of a cellular solid with a relative density of ~ 0.24 - 0.32 according to the scaling law where $\sigma_y = 0.3\bar{\rho}^{1.5}\sigma_{ys}$ ⁴⁹. Larger ligament sizes lead to a reduction in strength, with the precise mechanism still being a matter of ongoing discussion due to the complexity of the interplay between microstructure and free surfaces in the nanoporous foams ⁴⁹.

In contrast to the stochastic nature of the Au foams, the microlattices have an ordered and controllable geometry, which allows the exploitation of the “*smaller is ductile*” material size effect for some material systems ¹³. For example, Rys, et. al. showed that the compressive strength of NiP metallic glass microlattices with relative densities of 10^{-4} is an order of magnitude higher than that of nanocrystalline NiP microlattices with the same geometry ¹³. That work also demonstrated that these metallic glass hollow-tube micro-

trusses with 150nm thick tube walls deformed in a ductile fashion, in contrast to their thicker-walled counterparts, which undergo catastrophic failure upon loading. Such a transition in deformation mode from brittle to ductile has been reported for nano-sized metallic glasses and has been attributed to the energetic balance between shear band propagation and homogeneous deformation ^{2,13-16}. The authors also showed that the scaling of yield strength with density decreases from $\rho^{2.3}$ to $\rho^{1.4}$ when the wall thickness falls below 150 nm ¹³. Gu, et. al have shown that material size effects can also be exploited to enhance the strength and stiffness of solid tube lattices with relative densities between 40 and 80% with single crystalline regions within the ligaments ³². For lattices with relative densities above 50%, Gu, et. al observed a strength 1.8 times that of the bulk Cu as a result of the “smaller is stronger” size effect ³². This chapter aims to show that nanolattices can exploit both structural and material size effects that have been observed in previous work independently to tune the strength and stiffness of an ordered cellular solid of a given relative density.

3.4 Experimental Methods

Nanolattices in this work were fabricated using two-photon lithography with a 780nm femtosecond pulsed laser (Nanoscribe GmbH) ^{35-37,52-55}. This technique involves the constructive interference of two photons within a 3-dimensional voxel, which provides a sufficient amount of energy to cross-link the photoresist within the voxel ³⁵. The photoresist is placed on a substrate which is then mounted on a stage that can move in all directions with a resolution of $\pm 10\text{nm}$ and a maximum displacement of $300\mu\text{m}$. The cross-linked polymer sample can be of any geometry with features down to 150nm ^{37,55}.

The cross-section of the tubes in the nanolattices is elliptical, which is an artifact of the two-photon fabrication process, and the ellipticity of the individual tubes changes as a function of the lattice angle. The samples were developed in propylene glycol monomethyl ether acetate followed by an isopropyl alcohol rinse to isolate the polymer nanolattices, which were then sputtered with approximately 200-700nm of columnar grained Au at 3mTorr and 50W. The internal polymer scaffold was then exposed using a focused ion beam and removed using an O₂ plasma etch³⁹.

The transmission electron spectroscopy (TEM) image of the tube walls shown in **Figure 8**, confirms that the sputtered Au has a columnar structure, with the grains oriented orthogonally to the length of the tubes, which is consistent with the typical columnar grains on flat substrates⁵⁶⁻⁵⁸. The size of the grains ranged from 50 to 100nm when measured using a cross-section parallel the length of the columnar grains and 25-50nm when measured from a cross-section perpendicular to the length of the columnar grains (**Figure 8b**). All samples were designed to have octahedron geometry and a constant relative density, i.e., structures with thicker tube walls had larger unit cells. A geometric model was developed in SolidWorks and was used to predict the geometric parameters needed such that the relative density would be $\bar{\rho} \approx 0.02-0.04$ for all samples. After the samples were fabricated, the geometric parameters were measured using scanning electron microscopy (SEM) and these values were used in the SolidWorks model to calculate the relative densities of the fabricated nanolattices, which was found to be $\bar{\rho} = 0.05 \pm 0.01$. The mean and standard deviation for the relative density were calculated by averaging the relative densities of all fabricated samples, which was determined using SEM images for each fabricated sample. Thicker tube walls caused greater non-uniformity of the coating,

especially near unit cells along the edge of the nanolattice, and this is shown in **Figure 9**. For all samples, the wall thicknesses were measured from SEM images at multiple points along the height, width, and depth of the compressed regions of the nanolattice.

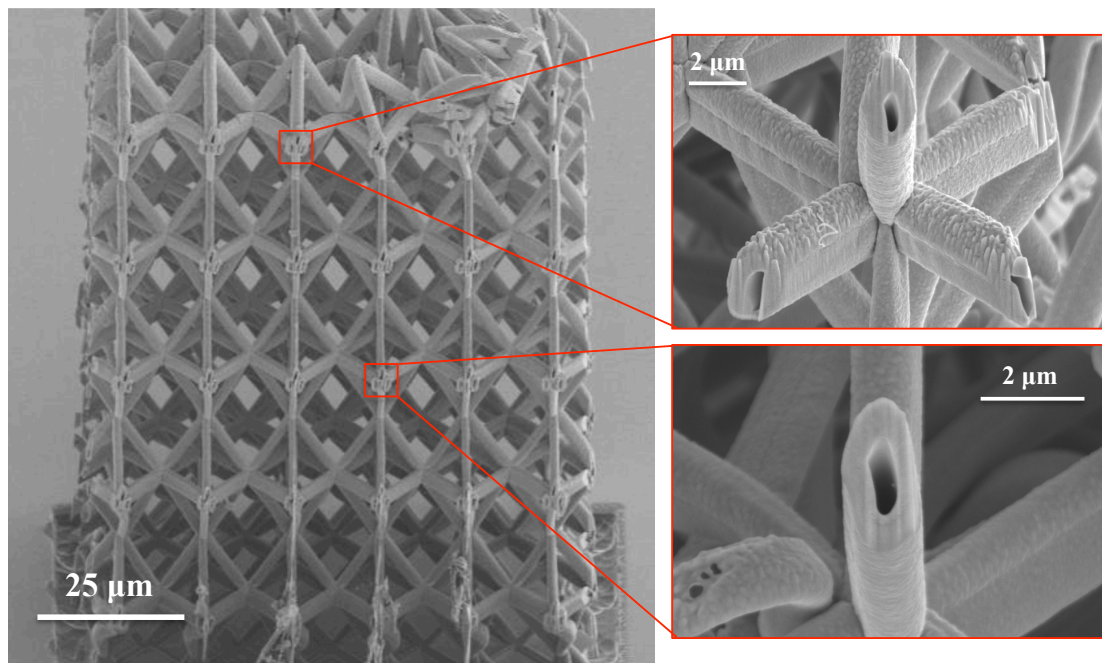


Figure 9: Representative images of the Au coating in a 60° nanolattice with a wall thickness of ~ 661 nm. In the center region, the nanolattice walls are conformal; however, the coating is not conformal near the edges of the lattice as a result of the anisotropy of the sputtering process.

To exploit structural effects, we fabricated and tested octahedron nanolattices with angles of 30° , 45° , and 60° , and a constant relative density of $\bar{\rho} = 0.05 \pm 0.01$. The lattice angle is defined in this work to be the angle between the horizontal mid-plane of the unit cell and the lattice tubes, consistent with previous work, and is shown in **Figure 8**. The wall thicknesses in these samples was $t = 336 \pm 58$ nm. The wall thicknesses presented in this work are in the regime where material size effects have been observed for nano-pillar geometries, which are discussed in the *Background: Material Size Effects* section. Material size effects were probed by varying the wall thickness for the octahedron geometry

nanolattices with constant relative density of $\bar{\rho} = 0.05 \pm 0.01$ and a fixed angle of 45° ; the same experiment was repeated for lattices with a fixed angle of 60° . Mechanical properties of the nanolattices were obtained by conducting uniaxial compression experiments in an in-situ nanomechanical instrument (InSEM, Nanomechanics, Inc.). Samples were compressed to strains of 40 to 60% at a constant prescribed strain rate of $\dot{\epsilon} = 10^{-4} \text{ s}^{-1}$ or lower and load-displacement data was collected. A diamond flat punch with a diameter of $170\mu\text{m}$ was used to compress the nanolattices. The effective stress was calculated according to $\sigma = F/A$ where F is the measured load and A is the total cross-sectional area of the nanolattice and the yield stress was calculated using the 0.2% offset method. The modulus was calculated using the slope from the elastic loading regime and was calculated using $\mathcal{E} = \Delta H/H$, where H is the height of the nanolattice and ΔH is the measured displacement. The unloading slope of the stress-strain curve was not used to determine the modulus of the nanolattice since the structures deform plastically and the unloading slope would give the modulus of the densified structure; initial regions where the sample may not have fully been in contact with the punch were excluded from the modulus calculation, though these were minimal across the data.

3.5. Results

3.5.1 Structural Effects

To determine the effect of geometry on the mechanical properties of the nanolattices, experiments were performed on octahedron unit cells with angles of 30° , 45° , and 60° . **Figure 10** shows SEM images of the nanolattices before and after compression, as well as stress-strain data for a representative sample for each lattice angle. A circle on the stress-strain curves denotes the yield stress for each of the nanolattices shown in **Figure**

10. Four samples were fabricated for each lattice angle and the 0.2% yield stress and modulus were found by averaging over all samples for each angle, and the data is shown in

Figure 11.

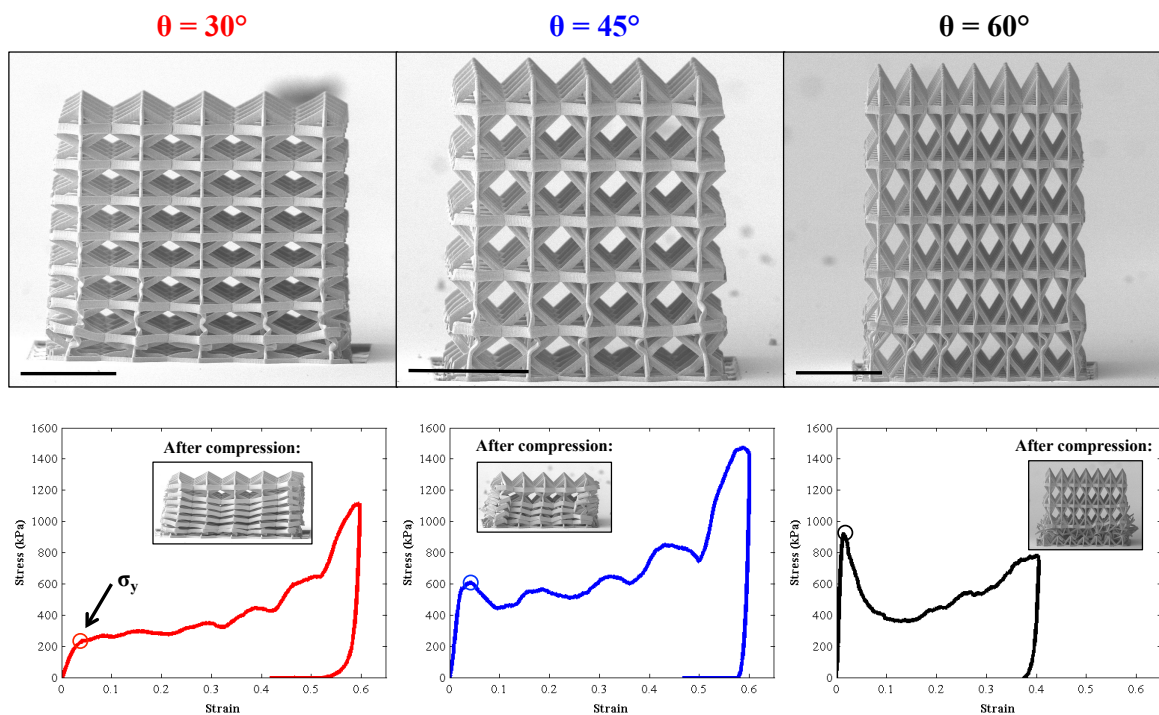


Figure 10: SEM image of octahedron nanolattices with lattice angles from 30° to 60° , as well as representative stress- strain curve for each sample; an open circle denotes 0.2% yield stress of the structure. For the 30° lattice, it should be noted that the error bars are included but are small enough to be obscured by the data point itself. (Scale bar denotes $30\ \mu\text{m}$)

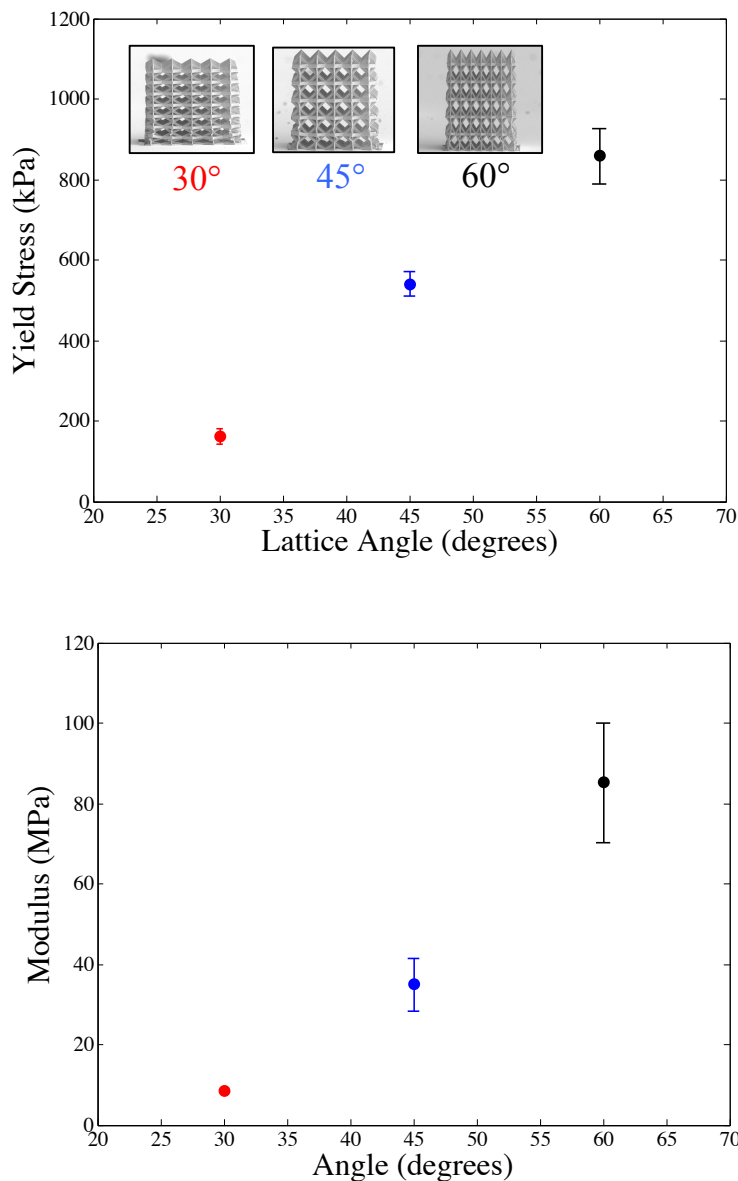


Figure 11: Calculated yield stress and modulus values for lattices with angles ranging from 30° to 60°. The error bars were calculated by using the standard deviation of the data for yield stress and modulus. (Note: $t = 352 \pm 87\text{nm}$ for all samples)

These plots show that higher angle in the unit cells leads to higher yield strength and stiffness. As the angle changes from 30° to 60° the yield stress increases from 161.3 ± 18.5 kPa to 858.2 ± 68.4 kPa, and the stiffness increases from 8.42 ± 0.7 MPa to 85.2 ± 15.0 MPa. The data also shows that the yield stress was reached at lower strains at higher lattice angles.

3.5.2 Material Size Effects

To examine the ability of nanolattices to exploit material size effects, uniaxial compression experiments were performed on the octahedral nanolattices with two different fixed lattice angles, 45° or 60° , and the wall thickness varied from $t = 200$ to 635nm . **Figure 12** shows the images of 45° nanolattices before and after compression, as well as the representative stress-strain data for each structure.

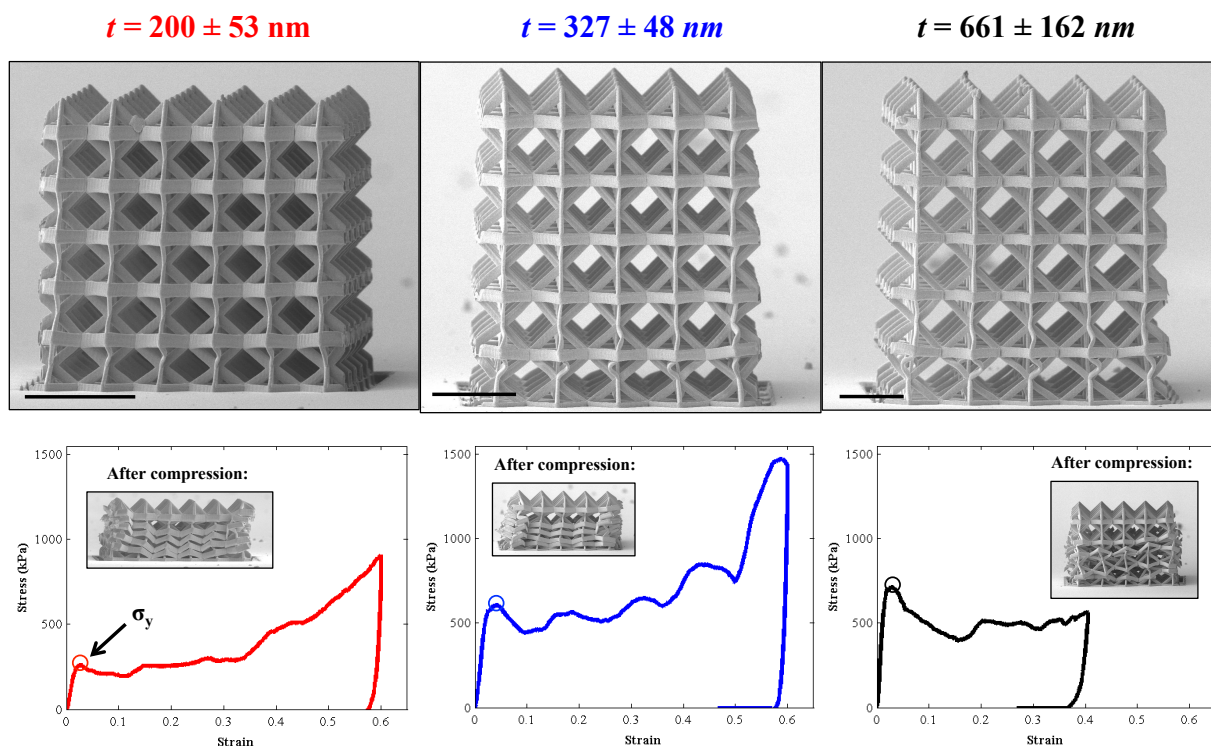


Figure 12: SEM image of 45° octahedron nanolattices with t ranging from 200 to 635nm, as well as representative stress-strain curve for each sample; an open circle denotes 0.2% yield stress of the structure. (Scale bar denotes $20 \mu\text{m}$)

For the 45° nanolattices, the yield stress was calculated by taking the average of 4 samples for each of the $t = 200\text{nm}$ and 327nm cases and 1 sample for $t = 635\text{nm}$ case. The data indicates that for the 45° nanolattices the yield stress increased by a factor of 2.1, or by $\sim 120\%$, as t increased from 200nm to 327nm and by $\sim 13\%$ as t increased from 327nm

to 635nm. The 0.2% yield stress increased with t but occurred at approximately the same strain for all 45° samples. Yield stresses were also calculated for nanolattices with a lattice angle of 60° for 2 samples with $t = 325\text{nm}$ and 1 sample with $t = 661\text{nm}$. The 60° nanolattices appeared to be ~58% stronger than the 45° nanolattice for all wall thicknesses, as shown in **Figure 13**, which is consistent with the results from literature ³⁴. The yield stress of the 60° nanolattices increased by ~14% as t varied from 325nm to 661nm. Yielding occurred at approximately the same strain of 1.2% for all 60° samples, which is lower than 1.7% yield strain in the 45° samples. The large error bars for tests on samples with the thickest walls, shown in **Figure 13**, is likely a result of the anisotropy introduced the sputtering process.

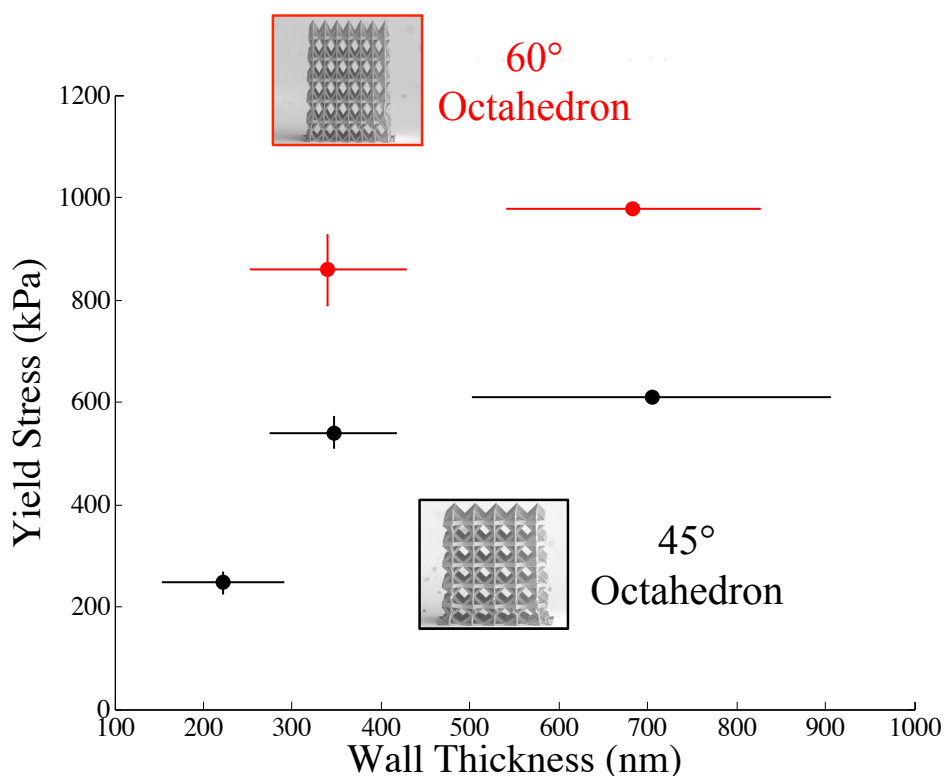


Figure 13: Calculated yield stress for both 45° and 60° octahedron nanolattices. The yield strength increases as (t/d) increases due to the material size effect.

All deformation initiates at the base of the nanolattice structures, where the coatings are more conformal compared to the top layer on unit cells, so the mean is a more representative wall thickness for the area of the nanolattice that deforms during the experiments.

3.6 Discussion

3.6.1 Critical Stress Criteria: Euler Buckling or Yielding of Lattice Struts

Building upon an analytic model proposed by Valdevit, et. al to calculate the stress required to initiate Euler buckling or yielding along the tubes for a microlattice with hollow circular tubes, we account for the hollow elliptical tubes in the octahedron lattice geometry presented in this work^{43,59}. Since changes in the geometric parameters of the nanolattices, such as wall thickness or tube diameter can lead to structural effects, the initial deformation of the tubes must be consistent across all samples with varying geometric parameters such that lattice angle and material size effects can be isolated. For example, under an applied load the lattice tube can either undergo Euler buckling or yielding of the constituent material as the tubes are compressed; as the geometric parameters of tubes, such as the length and wall thickness, are varied it may be possible to initiate buckling prior to yielding of the constituent material. To determine the critical stress to initiate Euler buckling, the following force balance is considered. P_{bar} is the force in each bar under an applied load, P_{applied} . The octahedron geometry has 8 bars that share the vertical load and 4 horizontal members. The horizontal members are neglected for the first-order analytic solution to find the stress at which Euler buckling occurs since they will not undergo Euler buckling due to their orientation with respect to the loading axis; only the 8

bars that carry the vertical load are considered in this derivation. For a representative unit cell denoting the geometric parameters, see **Figure 8**.

Sum of Forces:

$$\sum F = 8P_{bar} \sin \theta - P_{applied} = 0$$

$$P_{applied} = 8P_{bar} \sin \theta$$

$$\sigma_{applied} = \frac{8P_{bar} \sin \theta}{Area}; \text{Area} = L^2$$

When $P_{bar} = P_{cr}$ for Euler buckling, $\sigma_{applied} = \sigma_{buckling}$

$$\sigma_{buckling} = \frac{8P_{cr} \sin \theta}{L^2}$$

For Euler buckling:

$$P_{cr} = \frac{\pi^2 EI}{(kl)^2}$$

(assume $k = 1$ for pinned – pinned boundary condition)

The length of the bar can be related to the unit cell size by: $L = 2l \cos \theta \rightarrow l = \frac{L}{2 \cos \theta}$

$$P_{cr} = \frac{\pi^2 EI}{(kl)^2} = \frac{\pi^2 EI 4 \cos^2 \theta}{L^2}$$

Area moment for a hollow elliptical beam is:

$$I = \frac{\pi}{4} (D_{max} + t)(D_{min} + t)^3 - \frac{\pi}{4} D_{max} D_{min}^3$$

Neglecting higher order terms since t is small:

$$I = \frac{\pi t D_{min}^2}{4} (3D_{max} + D_{min})$$

As the wall thickness increases for the various samples, this assumption becomes less valid and high ordered terms should be considered in the buckling and yielding loads are of comparable magnitude.

Critical buckling load becomes:

$$P_{cr} = \frac{\pi^3 E t D_{min} \cos^2 \theta}{L^2} (3D_{max} + D_{min})$$

Critical stress to initiate Euler buckling in lattice members is:

$$\sigma_{buckling} = 8\pi^3 E \cos^2 \theta \sin \theta \left(\frac{D_{min}}{l}\right)^2 \left(\frac{D_{min}+3D_{max}}{l}\right) \left(\frac{t}{l}\right) \quad (\text{Eqn. 2})$$

To determine yielding criteria consider the compressive stress on the bar and ignore any bending moments which may result due to imperfections in the structure during the fabrication process. The compressive stress in the bar can be described by:

$$\sigma_{bar} = \frac{P_{bar}}{A_{bar}}$$

where:

$$A_{bar} = \pi(D_{max} + t)(D_{min} + t) - \pi D_{max} D_{min} = \pi t(D_{max} + D_{min})$$

$$P_{applied} = 8P_{bar} \sin \theta$$

Equating the yield stress of the constituent material, (nAu), to the applied load,

$$\sigma_{y(nAu)} = \frac{P_{applied}}{A_{bar}(8 \sin \theta)}$$

$$\sigma_{y(nAu)} = \frac{P_{applied}}{\pi t(D_{max} + D_{min})(8 \sin \theta)}$$

Rearranging and normalizing $P_{applied}$ by area of unit cell to get applied stress:

$$\sigma_{yield} = \frac{8\pi t(D_{max} + D_{min}) \sin \theta}{L^2} \sigma_{y(nAu)}$$

Rearranging:

$$\sigma_{yield} = 4\pi \sin \theta \left(\frac{t}{l}\right) \left(\frac{D_{min} + D_{max}}{l}\right) \sigma_{y(Au)} \quad (\text{Eqn. 3})$$

The geometric parameters (D_{min} , D_{max} , t , l) used to calculate the critical values to initiate Euler buckling or yielding of the nanolattice tubes are schematically defined in **Figure 8a** and tabulated for each sample in **Table 1**. The yield stress of the Au, $\sigma_{y(Au)}$, in **Equation 3** was measured via nano-indentation into 2.17 μm thick film on a glass substrate to a depth of 100-200nm to be $583 \pm 41\text{MPa}$, and the indentation modulus to be $E = 95 \pm 4\text{ GPa}$, both calculated using the Oliver-Pharr method ⁶⁰. The stresses required to initiate either yielding or Euler buckling in the Au nanolattices were calculated using **Equation 2** and **3** and are shown in **Table 2**.

Geometry	Angle	Thickness, t (nm)	Major Axis, D_{max} (μm)	Minor Axis, D_{min} (μm)	Tube Length, l (μm)	Thickness to Length Ratio, t/l	σ_{yield} (MPa)	$\sigma_{buckling}$ (GPa)
Octahedron $\rho = 0.05 \pm 0.01$	30°	357	2.68	1.31	7.97	0.05	164	12.5
	45°	200	2.39	0.80	4.77	0.05	290	16.4
		327	2.76	1.17	7.96	0.04	210	8.78
		635	3.21	1.65	11.12	0.06	259	10.6
	60°	324	2.71	1.18	9.71	0.04	170	2.41
		661	3.14	1.53	13.07	0.05	229	2.96

Table 2: Relevant average geometric parameters, as well as threshold stress values for both yielding and Euler buckling, for all samples.

The experiments presented in this chapter consider structures of constant relative density and lattice type, therefore the geometric parameters (D_{min} , D_{max} , t , l) of the hollow tubes must change with the wall thickness, t . As a result, all samples presented in this chapter have varying values of D_{min} , D_{max} , t , and l , which are shown in **Table 2** along with the critical stress to initiate Euler buckling and yielding. We found that for all nanolattices

in this work, the threshold stress for yielding was in the range between 164-290 MPa, which is more than an order of magnitude lower than that required for Euler buckling (2.4-16.4 GPa). Potential errors in the magnitude of the critical stress values may be introduced if size effects cause the value of $\sigma_{y(Au)}$ to vary as the wall thickness increases; however, based on previous work, an order of magnitude change in the yield strength of the Au is not expected due to size effects^{6,11}. This implies that all samples will fail by yielding upon compression and that any geometric changes required to keep relative density constant do not change the fundamental deformation behavior of the nanolattice tubes, when considering elastic buckling vs. yielding in compression along the tube length. We observed that the initiation of yielding always occurred at the hollow nodes because of the substantial local stress in all experiments. The analytic solutions presented demonstrate that yielding is far more favorable than buckling however the observed failure in the experiments results from plastic buckling of pre-bent tubes, as is the case for the collapse of the layer nearest to the substrate, or yielding at the nodes. The applied stress required to plastically deform a pre-bent beam or to initiate plastic deformation in an area with a high stress concentration, such as the node, is significantly less than both the applied stresses to initiate Euler buckling or yielding along the tubes. The dominance of nodal deformation within the structure renders minor non-uniformities within the wall thickness relatively inconsequential for mechanical behavior.

We found that the stresses predicted for the onset of yielding by **Equation 3**, within the range of 164-290 MPa, did not match the experimental data, which ranged from 161 – 976 kPa (see **Table 3**).

Lattice Angle	Wall Thickness (nm)	Measured Yield Stress (kPa)	Analytic Scaling Law: $\sigma = 0.3 \sigma_s \rho^{1.5}$ (MPa)	Measured Modulus (MPa)	Analytic Scaling Law: $E = E_s \rho^2$ (GPa)
45°	200	246	1.96	15.8	4.75
	327	540		34.9	
	635	610		56.0	
60°	324	858		85.2	
	661	976		77.0	

Table 3: Average measured and predicted yield stresses and modulus for the fabricated samples.

This discrepancy is likely caused by the fundamental limitations in the simple mechanics model in its inability to capture the complex stress state within the hollow structure. For example, the model accounts for buckling or yielding along the thin-shell hollow tubes with elliptical cross-sections but does not account for the complex geometry and stress state at the nodes where the tubes connect. The nanolattices experience higher stress concentrations at the nodes because the small radius of curvature where tubes converge induces the onset of yielding at the node instead of along the length of the tube. Our experimental observations and the analytic calculations confirmed that the deformation was consistently initiated by yielding at the nodes for all samples in this study. Valdevit, et. al. found that the analytic calculations for microlattices were approximately 1-2 orders of magnitude higher than those predicted by the FEM and than was observed experimentally, which is consistent with the observations in this work⁴³. A deviation of 1-2 orders of magnitude in strength has also been observed experimentally in micro- and nanolattices, and the deviation from the analytically predicted strength and stiffness in this

work is consistent with the existing literature^{31,40}. The tight distribution in the yield stresses in our experiments, shown in **Table 3**, implies that structural deformation in all samples likely occurred via yielding rather than buckling because this type of deformation is generally robust against defects. Buckling is an example of an instability phenomena where minor defects in the nanolattice geometry could significantly affect the critical stress required to initiate buckling and produce a wider spread in the data, which is not observed in these experiments⁵⁹. The low standard deviation observed across all data in this work is consistent with the prediction that failure of the tubes initiates by yielding based on the model proposed by Valdevit, et. al.⁵⁹. Experimental observations revealed that the sample first began to rotate and deform at the nodes prior to bending of the tubes, which may be induced by imperfections in the nanolattices.

3.6.2 Structural Effects

We found that the yield stress and modulus of the structures increase with the lattice angle of the unit cell (**Figure 11**). For the 30° case, the horizontal members of the unit cell carry more load in tension than would be experienced by the horizontal members in the 60° samples when a uniaxial force is applied to a sample based on a simple force balance. Alternatively, the vertical members of the 60° unit cell carry more load in compression than those of the 30° unit cell under the same uniaxial loading conditions. For beams loaded in tension, a slight pre-bend or misalignment has a much less significant effect on the mechanical behavior compared to a beam loaded in compression with an equivalent pre-bend or misalignment. As a result of the distribution of load across the unit cell as the lattice angle varies, it is expected that a larger standard deviation would be observed in the 60° samples and this is observed in the data.

The model proposed by Deshpande, et. al. that relates the modulus of a stretching-dominated pyramidal core can be extended to this work since the pyramidal core is half of the octahedron unit cell²⁰. Though the octahedron unit cell is a stretching-dominated structure, the octahedron nanolattices behave as bending-dominated structures due to rotation between and within unit cells as the lattice is compressed. This rotation is initiated by the initial imperfections in the unit cell layer closest to the substrate, which is a result of the polymer contraction that occurs during the development process. Minor imperfections and misalignments within the nodes of the octahedron nanolattices have been reported to induce lateral torsional bending in the nanolattice struts, which also contributes to the bending-dominated behavior observed in this work^{44,45}. The minor imperfections in the nanolattices, which are caused by the position accuracy of the two-photon fabrication system as well as the contraction of the polymer upon cross-linking, are an order of magnitude smaller than the unit cell size and account for the deformation mode of lateral torsional bending, as shown in existing literature^{44,45}. The trend in the data follows a modified form of the modulus relation proposed by Deshpande, et. al., shown in **Equation 4** and **Figure 14a**, to include the correct scaling for a bending-dominated structure

$$E = E_s \bar{\rho}^m (\sin \theta)^4 \quad (\text{Eqn. 4})$$

where $m = 2$ which is consistent with the theory classical theory for bending-dominated structures, where $E \propto \bar{\rho}^{2,22,41}$.

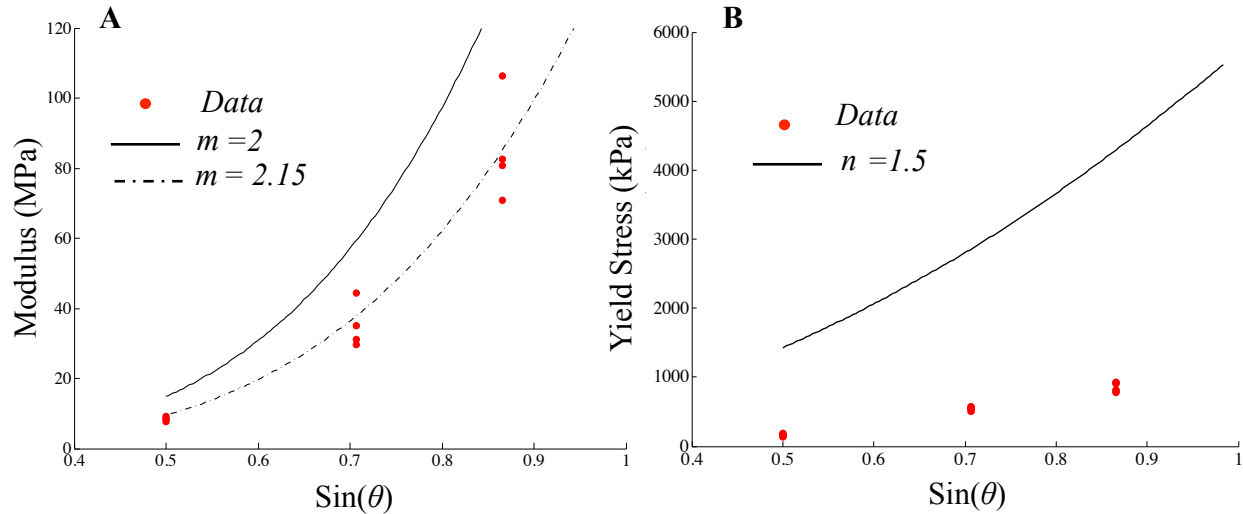


Figure 14: A) Modulus vs. Sine of lattice angle according to Eqn. 4; B) Yield stress vs. sine of lattice angle according to Eqn. 5.

Material size effects do not affect the modulus at these length scales, so $E_s \sim E$ of Au measured using nanoindentation. For bending-dominated structures where $E \propto \bar{\rho}^m$ with $m \sim 2$, the data also scales with $\sin^4(\theta)$ as predicted by literature; m of ~ 2.15 appears to provide a better fit to experimental data; however, to do a proper regression model to determine the best fit value for m , a wider range of lattice angles must be tested³⁴. The discrepancy in the relative density exponent is likely an artifact of the hollow nodes and it is expected that the nanolattices in this work would be less stiff than a cellular structure with solid nodes, which would scale with $m = 2$.

A similar analysis was done for the yield strength and compared to the predicted value for a stretching-dominated structure predicted by Deshpande, et. al.²⁰. A stretching-dominated pyramidal structure was predicted to scale as $\sigma = \sigma_s \bar{\rho} (\sin \theta)^2$ however a bending-dominated geometry, such as the octahedron nanolattices in this work, should scale as $\sigma \propto \bar{\rho}^{1.5}$ ^{20,22,41}. Modifying the model proposed by Deshpande et. al. to account for variation in the relative density exponent gives **Equation 5**.

$$\sigma = \sigma_s \bar{\rho}^n (\sin \theta)^2 \quad (\text{Eqn. 5})$$

Equation 5 captures the trend seen in calculated yield stresses for $n = 1.5$, shown in **Figure 14b**. The calculated yield stress deviates from that predicted using **Equation 5** by approximately an order of magnitude or more as the lattice angle increases. This is likely because of the hollow nodes and small imperfections, such as minor misalignment at the nodes or pre-bend in the unit cells connected to the substrate, all of which may emerge as a result of the fabrication process. The behavior of the lattice is more sensitive to imperfections as the lattice angle increase, as shown by the larger spread in the data at higher angles, and we attribute the increasing deviation from the predicted value, according to **Equation 5**, to this imperfection sensitivity at higher lattice angles. Material size effects alter the strength of the constituent material at the length scale present in the wall thickness of the nanolattices, however a model to describe this change in constituent properties for this geometry and microstructure is outside of the scope of this work. The $\sigma_s \bar{\rho}^n$ term acts as a constant in the yield stress $\sim f(\sin(\theta))$ relation therefore the value of n cannot be determined until the microstructure and material size effects present in the nanolattices are further characterized. The deviation in the m and n values from that which is expected of a bending-dominated structure ($m = 2, n = 1.5$) is likely due to the complex stress state at the hollow nodes that initiates failure well below analytically predicted values. The scaling laws for cellular solids assume pin-jointed structures, which is not the case for the fabricated samples presented in this work, and therefore it is expected that the m and n values would deviate from those predicted using analytic theory^{22,41}. Additionally, deviations of up to an order of magnitude between experiments, models, and analytic predictions for strength have been observed in previous work⁴³.

3.6.3 Material Size Effects

The yield strength of the Au tube walls is expected to be lower than that of the same material in monolithic form because the nanolattices in this work have wall thicknesses in the range where the reduced sample dimensions can lead to weakening in metals with nanometer-sized grains^{1-6,10-12}. The applicability of the model proposed by Gu, et. al in **Equation 1** to the nanolattice system is limited because the tube walls of the nanolattices are effectively a freestanding thin film in which the grains are confined laterally, although multiple grains may also span the wall thickness. The thickness of the nanolattice walls, t , and the microstructure of constituent material are relevant parameters for predicting the strength of the hollow Au tubes. The nanolattices in this work represent an interconnected system of such tubes and demonstrate that the material size effects observed in a simple nanopillar geometry can be exploited to control and tune the mechanical properties of the entire structure. Though a model to describe the material size effect is outside the scope of this work, any geometric parameters that potentially cause structural effects or changes in relative density are held constant and the structures are self-similar as wall thickness increases, so we attribute the observed lower yield stress to changes in the microstructure of the constituent material as the wall thickness dimension decreases. **Table 3** shows the predicted yield stress and modulus of a structure with a fixed geometry and relative density, assuming the constituent material properties are constant, as well as the measured yield stress and modulus. The discrepancy in the measured and analytically predicted values is 1-2 orders of magnitude, which may be attributed to the complex stress state at the hollow node and imperfections in the lattice due to the fabrication process. The scaling laws of Gibson and Ashby predict a constant yield stress for all structures, yet this work

demonstrates that tuning the microstructure of the constituent material and its dimensions at small length scales enables tuning the strength in the fabricated nanolattice structures⁴¹. Increasing the lattice angle from 45° to 60°, we observe an improvement over the lower angle case by ~1.6 times for multiple wall thicknesses and again show the tunable strength of the nanolattices as a result of material size effects.

The 45° nanolattices were nominally conformally coated with a ~200nm-thick Au. TEM analysis revealed that these 200nm-thick films were more porous than samples with thicker walls. This is likely due to the porosity of the polymer onto which the Au is deposited; the 200nm thick walls were the thinnest conformal layer possible with the sputtering technique and the pores within the thin walls are shown in **Figure 15**.

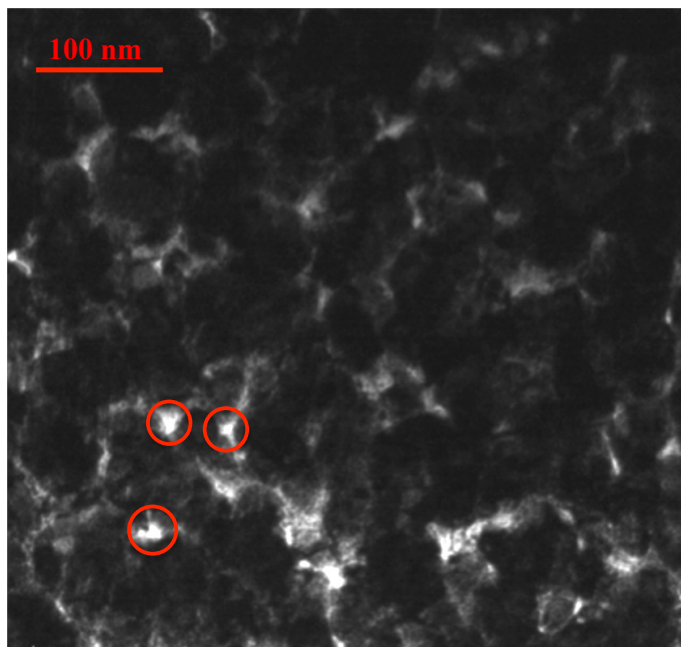


Figure 15: TEM bright field image showing pores between grains as viewed through a section of a nanolattice wall where the wall thickness is ~200nm.

Thicker films had no observable pores, as revealed by TEM and ion channeling of ~2 μ m n-Au thin films deposited under identical conditions, shown in **Figure 16**. This

decrease in porosity as t increases is consistent with the mechanisms for polycrystalline film growth on a substrate where the nucleation sites grow to coalesce into a fully dense thin film⁶¹. The greater porosity impacts the mechanical response of the film because at low wall thicknesses the tubes of the nanolattices act as a thin film with defects rather than a fully dense constituent material. The films that comprise the nanolattice tubes are oriented at an angle to the loading direction, as defined by the lattice angle, so it is expected for the structures to be weaker when loaded in this configuration compared to loading applied along the length of the columnar grains. We propose this to be the cause of the large change in both yield stress and modulus as t increases from 200nm to 327nm. Ion channeling and TEM confirm that as the wall thickness increases, more grains span the thickness of the film, as shown in **Figure 16**; however, there are single grains that may span the thickness of the nanolattice wall.

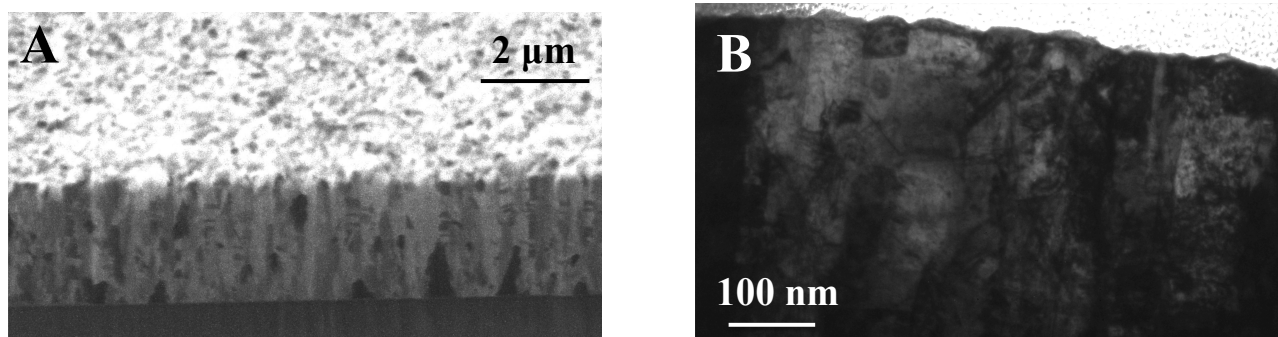


Figure 16: A) Ion channeling (sample at 52° tilt) and B) TEM images of a ~2μm thin n-Au film showing columnar grain structure with multiple grains spanning the film thickness.

Additionally the average height of the grains is on the order of ~100nm so it is suspected that for $t = 200\text{nm}$ there are fewer grains that span the thickness of the film; however, as t increases more grains span the thickness and the behavior approaches that of the bulk constituent Au. The data for the 45° nanolattices shows a significantly larger

increase in yield strength as t increased from 200 to 327nm compared to the increase in yield strength as t increased from 327 to 635nm, where there is no porosity. This suggests that the strength of the constituent material is approaching the bulk value for $t > 327$ nm, which is also consistent with the literature for nanocrystalline nanopillars with increasing ratios of (t/d) ^{6,10,11}. Existing models for thin films or nanopillars geometries are not directly applicable to this work since the stress state of the hollow nanolattice structures is complex and the microstructure varies as a function of wall thickness. Characterizing the deformation mechanism of the constituent material at varying wall thicknesses is the subject of future work to further understand the deformation mechanism of hollow metallic nanolattices at all length scales.

3.7 Conclusions

Hollow Au octahedral nanolattices with variable wall thicknesses and lattice angles were fabricated and it was discovered that upon uniaxial compression, structural and material size effects could be utilized to tune strength and stiffness. Without inducing a change in deformation mechanism of the lattice tubes, changes in the lattice angle can increase both the yield strength and modulus of the lattice by approximately an order of magnitude. Tuning the wall thickness of the nanolattices makes it possible to exploit material size effects of the small-scale constituent material, thus increasing the yield strength by a factor of 2. Classical mechanics of cellular solids predicts a constant strength and stiffness for all nanolattice geometries explored in this study; however, by utilizing material size effects, the strength of a lattice with a constant deformation mechanism and relative density can be increased by up to a factor of 2. Exploiting structural effects can

provide up to an order of magnitude increase in strength and stiffness for a nanolattice with a constant deformation mechanism and relative density. We show that by exploiting the structural and material size effect parameters of nanolattices, the strength and stiffness of these cellular solids is no longer constant for a given deformation mechanism and relative density, as predicted by classical theories. By combining an understanding of structural mechanics and the behavior of small-scale materials, technology development is no longer limited by the constraints of existing cellular solids and new materials can be designed to meet the needs of emerging technology by exploiting structural and material size effects to tune mechanical properties.

Chapter 4: Insensitivity to Flaws Leads to Damage

Tolerance in Brittle 3D Architected Meta-Materials

Adapted from:

Montemayor, L.C., Wong, W. H., Zhang, Y. W., Greer, J.R. "Insensitivity to Flaws Leads to Damage Tolerance in Brittle 3D Architected Meta-Materials". (2015) In Preparation.

4.1 Introduction

Bulk ceramics are highly sensitive to flaws and fail catastrophically upon applied loads, most commonly at the small internal flaws like cracks, voids, and inclusions¹⁻³. Fiber-reinforced ceramic-matrix composites (CMCs) have been developed to reduce their sensitivity to flaws while capitalizing on the high strength of ceramics⁴⁻⁷. These CMCs utilize deformation of the matrix and/or fibers to delocalize strain near stress concentrators, such as holes or notches, which leads to flaw insensitive behavior^{4,5,7}. Insensitivity to notches has been reported for silicon carbide/calcium aluminosilicate CMCs for ratios of notch to sample size of $0.2 < (a_0/b) < 0.8$, where a_0 is the notch size and $2b$ is the sample width^{5,7}.

It has also been postulated that reducing sample dimensions of brittle materials can give rise to flaw insensitivity and to attain near-theoretical strength⁸. Gao, et. al.'s theoretical work demonstrated that a thin plate with a penny shaped notch exhibits the fracture strength of a perfect crystal when the plate thickness falls below a critical length scale, which is a function of surface energy, elastic modulus, and ideal material strength⁸. Nano-fracture experiments and computations on brittle nanocrystalline platinum nanopillars, with diameters of 100nm and a grain size of 6nm, revealed that their failure

strength remained equivalent to the ultimate tensile strength even in the presence of pre-fabricated flaws and that failure location was uncorrelated to the presence of the flaws⁹. This emergence of flaw insensitivity in nano-structures was attributed to their failure at the “weakest-link,” be it at an internal, microstructural stress concentration like a grain boundary triple junction or at an external flaw, with failure mechanism representing the intrinsic material strength. In the absence of a discrete material microstructure, it has been reported that 75nm-diameter metallic glass nanopillars containing external notches always failed at those locations at lower peak loads than their un-notched counterparts¹⁰.

These examples demonstrate that failure tolerance of some materials to flaws cannot be solely attributed to the length scale; it stems from the complex interplay between the internal microstructural energy landscape within the material and the external sample dimensions and geometry¹⁰. Several studies have demonstrated that incorporating architecture in material design enables proliferating lucrative material size effects that emerge at the nano-scale onto macro-scale architected meta-materials; for example *smaller is stronger/weaker* for metals, *smaller is ductile* for brittle metallic glasses, and *smaller is tougher* for ceramics¹¹⁻²⁸. The periodic arrangements of small-scale ordered cellular solids, such as nano- or meso-lattices, span length scales ranging from hundreds of microns to tens of nanometers and facilitate the attainment of novel mechanical properties under compression, like recoverability and enhanced specific strength compared to bulk, and these properties arise as a result of structural and material size effects^{26,27,29,30}. Existing cellular solids theories predict that mechanical behavior is determined by the deformation mechanism of the lattice, which is either by bending or stretching and is a function of the nodal connectivity, and the constituent material properties³¹⁻³³. A bending dominated

structure is predicted to have lower strength and stiffness when compared to a stretching-dominated structure³¹⁻³⁴. In the case of architected bulk materials, another aspect of microstructure arises in the dimensions of not only the grains of the constituent material but also in the size of the unit cells. Fracture experiments on macro-scale cellular solids have been explored in literature; tensile properties of nanolattices – with or without pre-fabricated defects - are currently unknown^{32,35-42}.

We explore tensile failure of 3-dimensional hollow alumina kagome nanolattices and demonstrate that they exhibit flaw tolerance in terms of strength and failure location, which we attribute to the presence of a discrete structure at the micron and sub-micron lengths scales within a continuum-like material.

4.2 Fabrication of Hollow Kagome Tension Samples

We performed uniaxial tension experiments on hollow alumina (Al_2O_3) nanolattices with and without through-thickness notches. **Figure 17** shows the CAD design and SEM images of an as-fabricated dog-bone-shaped hollow alumina kagome nanolattice thin plate embedded in an octet-truss lattice head; the kagome lattice had a unit cell size of $l = 3.85 \pm 0.16 \mu\text{m}$, the octet-truss head had a unit cell size of $l \sim 4.5 \mu\text{m}$, shown in **Figure 17 (B and F)**. The kagome lattice was created by tessellating pairs of stacked tetrahedra in three dimensions in a hexagonal tessellation pattern, which gives rise to an A-B-C stacking pattern. The kagome unit cell shown in **Figure 17 (C and G)** contains a single complete set of A-B-C stacked tetrahedra. The tension samples were fabricated on a silicon wafer using a polymer scaffold created via two-photon lithography direct laser writing process and were subsequently coated with 50nm of Al_2O_3 using atomic layer deposition (ALD) at 150°C to make a composite Al_2O_3 /polymer structure. The octet-truss head had a width of $w = 139.8$

$\pm 1.1 \mu\text{m}$, a height of $h = 19.2 \pm 0.2 \mu\text{m}$, and a thickness of $t = 24.5 \pm 0.3 \mu\text{m}$, with the averages representing 5 samples. The Al_2O_3 /polymer kagome test section initially had a width of 12 unit cells, a height of 6 unit cells, and a thickness of 2 unit cells but the width was reduced at a later step in the fabrication process to accommodate the experimental set-up. The samples had an octet-truss lattice at both the top and bottom of the kagome test section, shown in **Figure 17 (A and E)**; a kagome A-B-C unit cell layer was embedded in octet-truss head and $\sim 5\mu\text{m}$ of the kagome test section was embedded in the bottom octet-truss lattice at the interface between the sample and the silicon wafer. The kagome lattice was embedded in the octet-truss lattices at the top and bottom of the test sections to avoid delamination at the interfaces between the kagome test section and the octet-truss head/substrate under tensile loading.

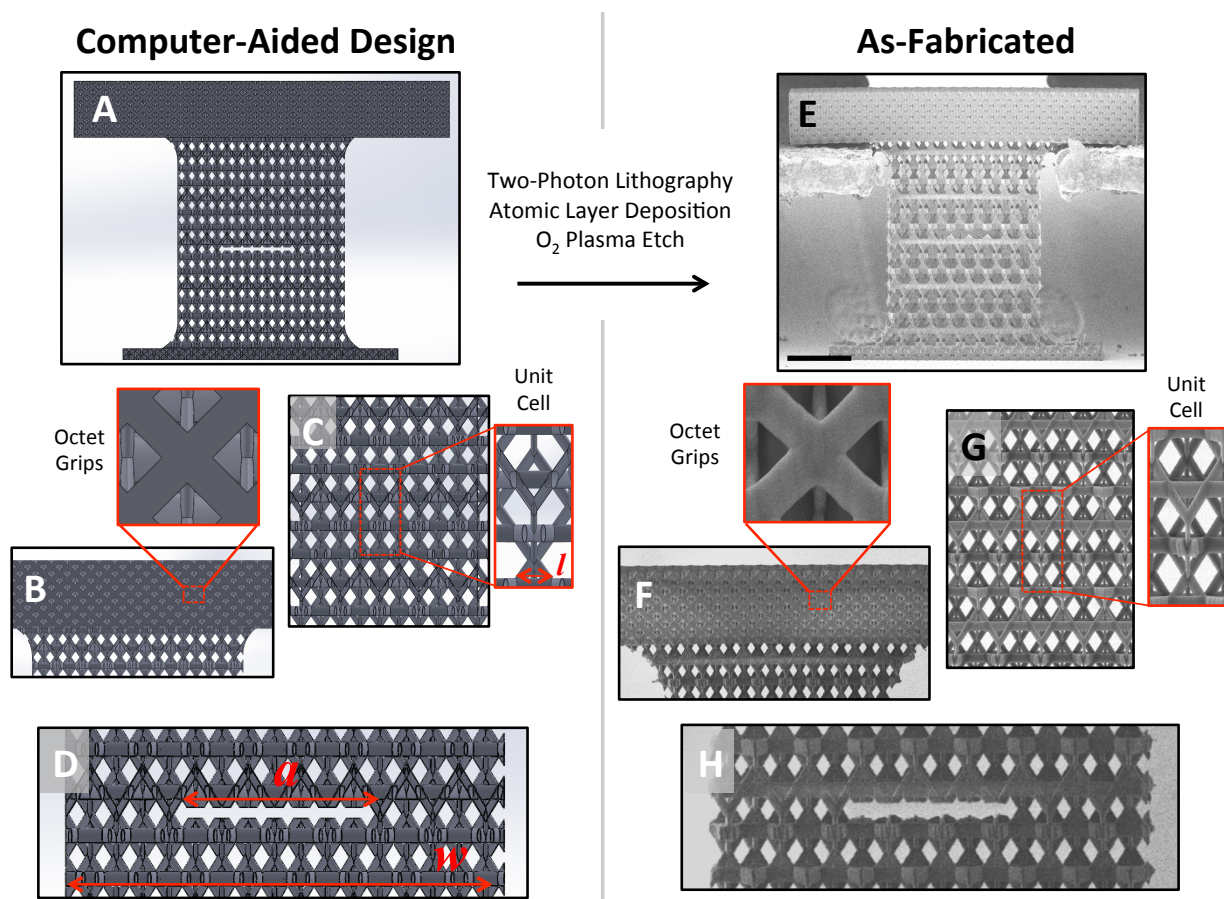


Figure 17: Representative notched nanolattice tensile specimens, designed in Solidworks (A) and as-fabricated samples (E).

The fabricated and designed unit cells, whose size denoted as l , are shown in (C) and (G), respectively. The grip used to apply uniaxial tension to the samples is an octet-truss lattice, shown in (B) and (F). The notch is shown in (D) and (H) and is denoted by the variable a while the sample width is denoted by w . Scale bar in (E) denotes 25 μm .

Samples were shaped into dog-bone tensile geometries using a focused ion beam (FIB), at a current of 7 nA, to have a curved edge at the kagome/octet-truss interfaces that served to reduce stress concentrations (**Figure 17 (B and F)**). The plate-like kagome Al_2O_3 /polymer test section had a final width of $w = 66.3 \pm 5.2 \mu\text{m}$, a height of $h = 81.9 \pm 0.3 \mu\text{m}$, and a thickness of $t = 15.4 \pm 0.5 \mu\text{m}$; the width and height averages were calculated using all samples presented in this work ($n = 18$) and the average thickness was determined by averaging the thickness of 10 representative samples after the deformation.

The FIB was also used to pattern the notches (**Figure 17 (D and H)**). We tested samples with notch lengths, a , ranging from 0 to 34.94 μm , and (a/w) varying from 0 to 0.54, where w is the width of the test section; the unit cell size was kept constant for all samples and notch length-to-unit cell size ratio, (a/l) , was varied from 0 to 9.1. Once the samples were shaped into their final geometry, the internal polymer was removed using O_2 plasma (16-18 hours at 100W) and the samples were visually inspected in the scanning electron microscope (SEM) to non-destructively determine the amount of polymer remaining in the sample (see Supplementary Info). When the Al_2O_3 kagome nanolattices were fully hollowed out, the octet-truss head remained a composite, containing the Al_2O_3 layer and the internal polymer. Additional details on the fabrication process can be found in Refs^{26,27,29,30,43}.

We chose the 3D kagome geometry because of its high predicted fracture toughness in 2D, which stems from elastic blunting near the crack tip^{32,40}. The hollow kagome nanolattices in this work are designed to have a stiffness of $E = 45$ MPa and a relative density of $\bar{\rho} = 0.02$, calculated using a Solidworks model of the kagome unit cell, shown in **Figure 17**, and the measured sample dimensions from SEM images. We chose the denser Al_2O_3 /polymer octet-truss lattice as the sample head to stiffen this section relative to the hollow kagome test section^{32,34}. The composite Al_2O_3 /polymer head has a 760x higher stiffness of $E = 3.90$ GPa and a relative density of $\bar{\rho} = 0.38$ (see Supplementary Info for details). We find that this difference in stiffnesses was sufficient to perform the tensile loading with minimized deformation of the octet-truss head.

4.3 *In-Situ* Uniaxial Tension Experiments and Simulations

The as-fabricated kagome dog-bone specimens were subjected to displacement rate-controlled uniaxial straining in an in-situ nanomechanical instrument, InSEM (Nanomechanics, Inc.), at a quasi-static strain rate of $\dot{\epsilon} = 10^{-3} s^{-1}$. Contact with the samples was made via a tension grip at the bottom faces of the octet-truss head on either side of the kagome lattice; the tension grip was milled in the head of a 0.8mm stainless steel screw using electrical discharge machining (EDM), as shown in **Figure 17E**. Load-displacement data, as well as real-time video of the deformation, was captured during each uniaxial tension experiment. The displacement of the gauge section was calculated using the observed length change, Δl , in the deformation video; uniaxial strain was defined as $\epsilon = \Delta l/l$, with the original length l measured in SEM prior to the experiment. The stress at failure was defined as $\sigma = F/A$, where A is the overall cross-sectional area of the sample and F is the measured force at failure. The slope of the unloading curve is not a reliable measure of the energy release-rate of the Al_2O_3 kagome nanolattice since the slope is an artifact of the InSEM controller.

Finite Element (FE) simulations of the as-designed notched and un-notched hollow kagome lattices were performed to assess the ability of continuum-based models to predict deformation of architected meta-materials. The samples in FE models were created from the SolidWorks-constructed geometries and accounted for the interface between the octet-truss sample head and the InSEM grips. Three-dimensional 3-noded triangular shell elements with reduced-integration were employed. The material properties of Al_2O_3 for the FE analyses were obtained from bulge experiments of equivalently deposited thin films of ALD Al_2O_3 , with the modulus, E , ranging from 164 to 165 GPa and the ultimate tensile strength, σ_{UTS} , in the range of 1.57 – 2.56 GPa; for the simulations in this work, the input

modulus and UTS were taken to be 165 GPa and 1.57 GPa, respectively⁴⁴. A linear post-cracking stress-strain relationship was incorporated in the simulations to represent the brittle behavior of Al_2O_3 . Displacement-controlled boundary conditions were applied to the octet-truss sample head in locations closely resembling the experimental setup. For numerical efficiency, explicit dynamics procedure was adopted to model the quasi-static applied uniaxial tension loading. To ensure a quasi-static response, the energy balance of the modeling system was constantly monitored such that the kinetic energy of the system was negligible compared to its internal energy and external work. Computations were performed within the finite strain setting using the general-purpose finite element program ABAQUS/Explicit Version 6.13.2. To model and reflect a quasi-static solution, the kinetic energy of the deforming kagome lattice was monitored and enforced to not exceed 1% of its internal energy throughout the majority of the quasi-static analysis. The studied (a/w) ratios were: 0, 0.11, 0.23, 0.35, 0.47 and 0.54. A constant wall thickness of 50nm across all elements was assumed for all simulations. The global stress and strain of the FE kagome test section was calculated using the same methodology as in experiments.

4.4 Results

Figure 18 shows SEM images and representative load vs. strain-to-failure data for the as-fabricated and notched geometries and reveals that all samples failed instantaneously and catastrophically, as expected for a brittle ceramic.

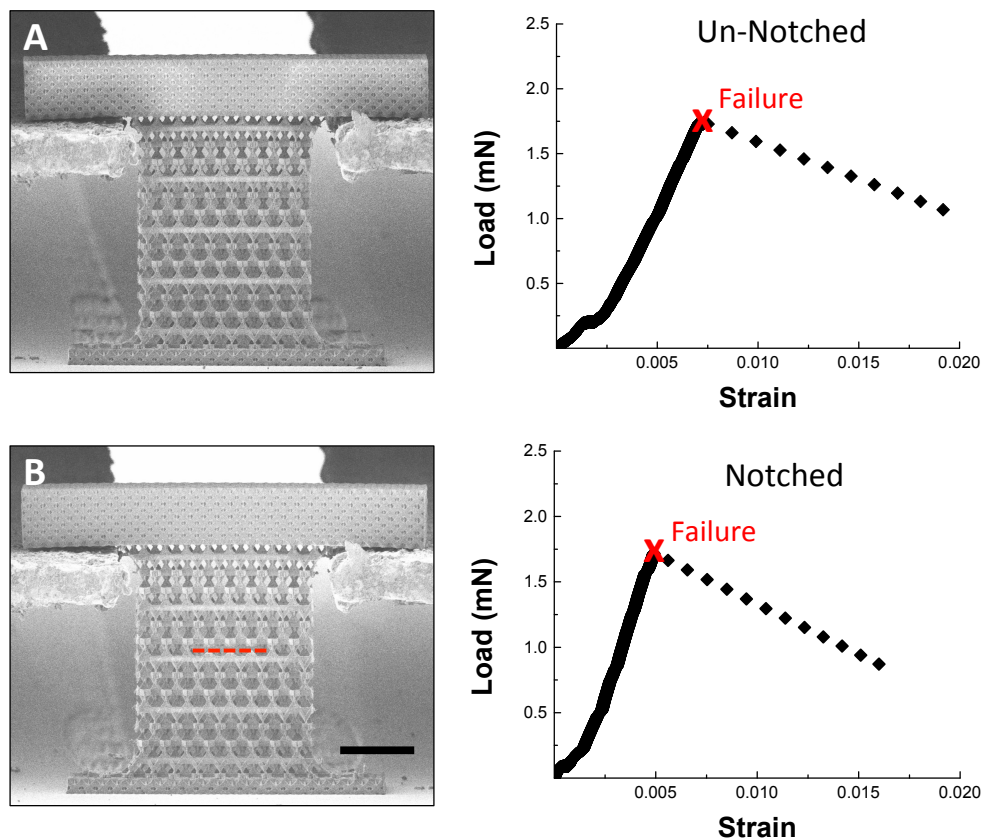


Figure 18: Representative load-displacement curve for un-notched (A) and notched (B) kagome nanolattices in uniaxial tension.

The dimensions of the notched and un-notched samples shown are identical with the exception a notch, which spans 1/3 of the sample width and is denoted by a red dashed red line. The red “X” denotes brittle, catastrophic failure and all data collected after this point is an artifact of the testing instrument and not representative of the measured load on the sample. Scale bar denotes 25 μ m.

Three un-notched samples ($a/w = 0$) had a $F_{peak} = 2.00 \pm 0.19$ mN and a strain at failure of $\epsilon_{failure} = 0.006 \pm 0.001$; the results for various notch sizes are tabulated in the Supplementary Information. **Figure 19** shows peak-load-at-failure data for samples with notch-to-width ratios, (a/w), spanning from 0 to 0.54. Samples with (a/w) between 0 and 0.32 had a relatively constant peak-load-at-failure of ~ 2 mN, which is equivalent to the peak load for the un-notched samples. The peak load decreased by 32% as (a/w) increased from 0.32 to 0.54, likely caused by the 4.2x higher compliance in the widest-notched samples when compared to un-notched samples, also shown in **Figure 19**. The experimentally

obtained peak load remained nearly constant over the (a/w) range of 0 to 0.32; the simulations show a monotonic reduction in the peak load with increasing (a/w) , decreasing by 59% as (a/w) widens from 0 to 0.35. The simulations also show a 1.5x increase in compliance as (a/w) increases from 0 to 0.54, slightly lower than that observed experimentally.

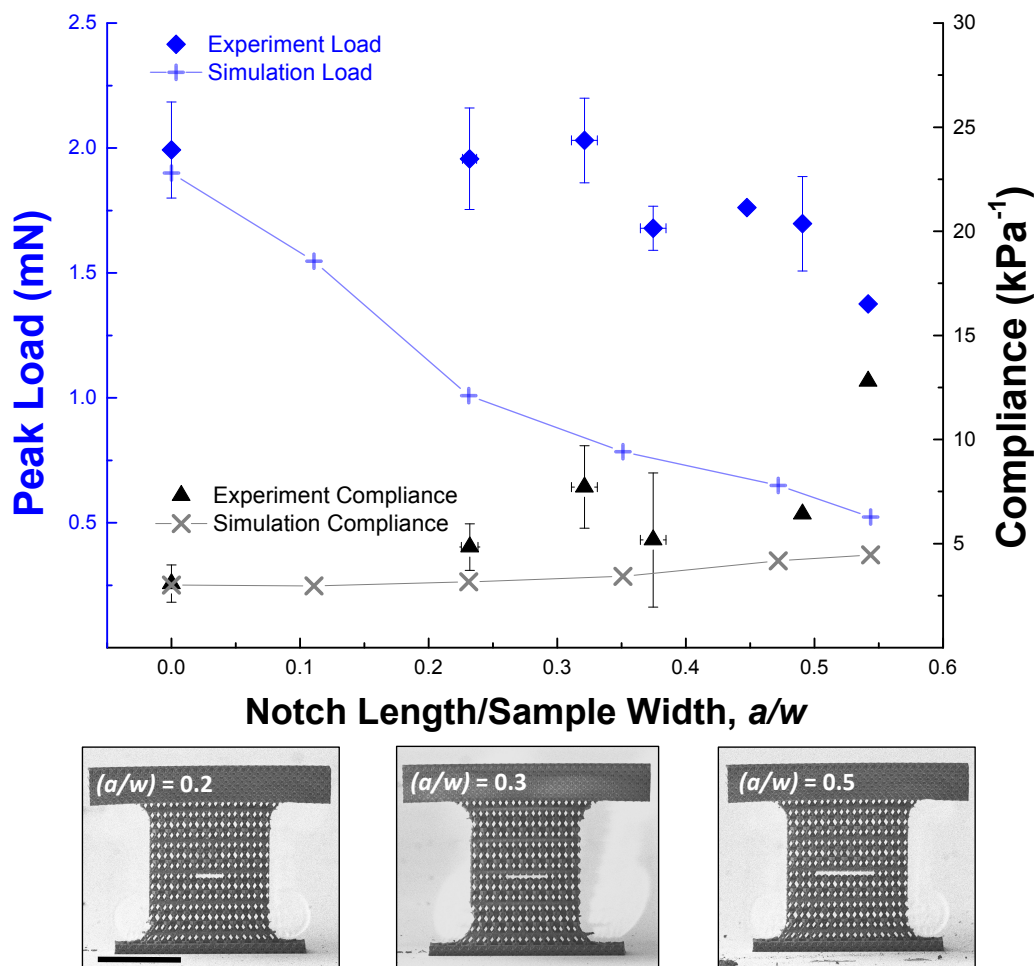


Figure 19: Comparison of finite element and experimental data for $4\mu\text{m}$ kagome lattices in uniaxial tension. Scale bar denotes $50\mu\text{m}$ in all images. The error bars in the experimental data were calculated using the standard deviation of the measured load and notch/sample dimensions; substantial errors were likely caused by the variations in the compliance of the sample head.

The sample compliance was calculated as $C = \epsilon/\sigma$, where σ is the applied load divided by the full cross-sectional area of the gauge section, A , for both experiments and simulations.

The experimentally measured compliance is the combined compliance of the sample/nanoindenter system and may not serve as a reliable measure of the absolute compliance of the nanolattices; the calculated compliance serves to compare the relative changes in sample compliance with increasing ratios of (a/w) .

4.5 Discussion

All samples in this work failed catastrophically for all (a/w) , with failure always occurring along a plane of nodes between the tetrahedral pairs forming the kagome lattice. FE simulations revealed that the highest local Von Mises stresses occur at the nodes, along the “planes” where the tetrahedra connect; **Figure 20** shows these calculations for representative un-notched and notched ($a/w = 0.3$) samples and reveals that the nodes serve as the weakest links when the nanolattice is tensed. This is not surprising, as it has been previously demonstrated that the nodes in similarly-made Al_2O_3 nanolattices were the weakest links and served as failure initiation locations in compression^{26,27}. We discovered that the as-fabricated, un-notched samples have equivalent local stresses in the nodes located in sample-interior and at the edge of the sample and that the notched samples have the highest local stress concentrations at the notch roots, with minimal local stress at the sample edge immediately prior to failure. Failure in each sample initiated at the node(s) that had a missing neighbor, whose detached side was not constrained by the neighboring unit cells in the lattice. Failure in the notched samples always initiated at the notch root where the adjacent unit cell had one constrained and one un-constrained boundary.

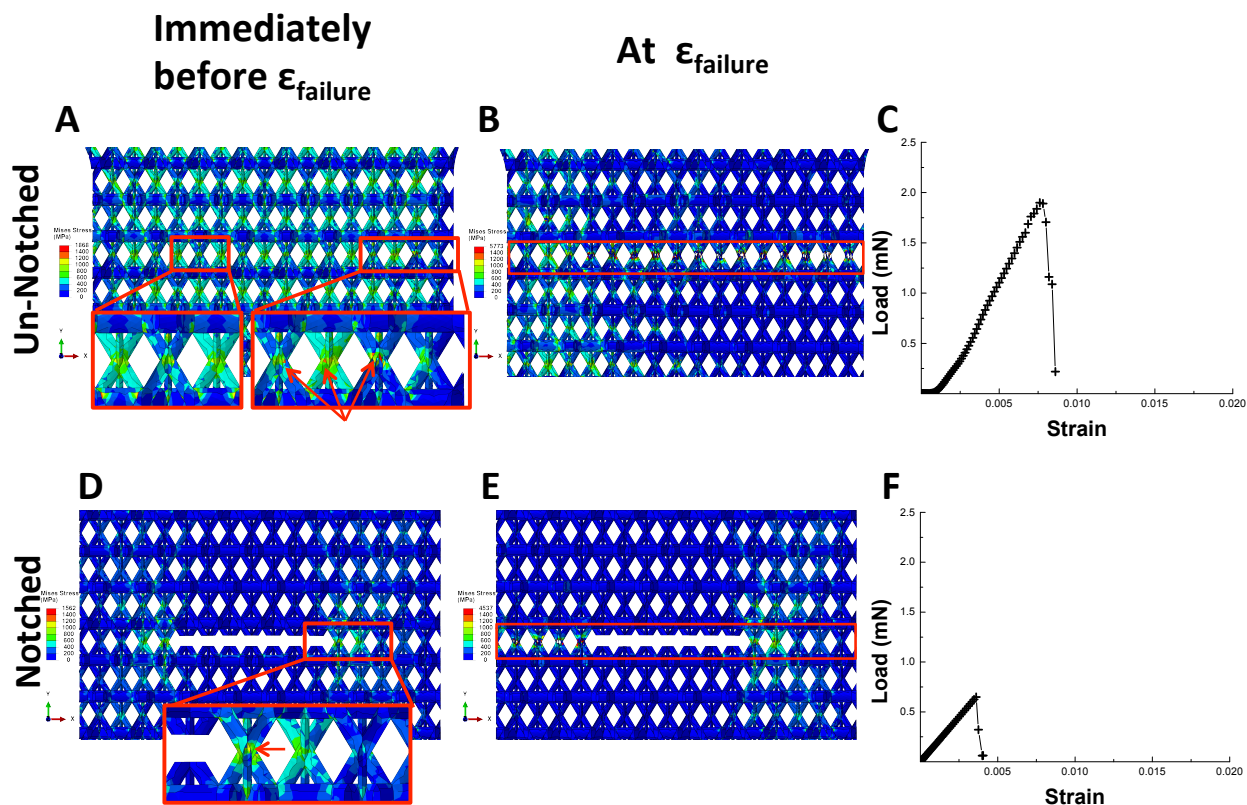


Figure 20: Finite element simulations show that the highest local Von Mises stress concentrations within the nanolattice occur at the nodes for both the notched and un-notched specimens. Red boxes denote the plane where failure occurs in (B) and (E).

All samples in this work had one edge containing unit cells that were fully disconnected from their vertical neighbors while the other edge had unit cells with minimal intact vertical connections along the sample edge; this is a result of the lattice unit cell size and the sample width required to fit the tension grips. Failure in all un-notched samples initiated at the edge with completely disconnected unit cells, where the local boundary conditions are similar to the case of the notched specimens. After incipient failure in a single edge node, the crack propagates instantaneously and causes catastrophic failure of the entire structure; the applied force required to fail the first node in uniaxial tension corresponds to the peak load at failure for a nanolattice.

While continuum-based classical mechanics theory predicts that the peak load will decrease at higher (a/w) ; the nanolattices here exhibit a nearly constant peak load of $\sim 2\text{mN}$ for $(a/w) < 0.38$, a value equivalent to that of the un-notched material^{1,2,45,46}. In monolithic ceramic materials with the same geometry, the stress concentration at a notch is highest because the external notch is significantly larger than the size of the internal microstructural flaws¹⁻³. Our simulations indicate that in a nanolattice, the stress concentrations at the nodes (internal) and at the notch (external) have similar magnitude because they both arise from the discrete nature of the periodic unit cells. These findings are consistent with tension experiments on notched nanocrystalline Pt nano-tension specimens, which show that the internal stress concentrations at triple junctions and at grain boundaries are comparable to the stress concentrations at the external notches⁹. The constancy of the peak load at failure arises from the global deformation in all samples being governed by single-node failure in uniaxial tension¹. As (a/w) increases to above ~ 0.38 , the observed peak load decreases, likely because the remaining intact unit cells are less constrained and experience bending moments. Fleck, et al. used FE simulations to show that 2D kagome lattices with solid beams exhibit elastic blunting at the crack tip that results from the stretching-periodic bending geometry, where the lattice bars deform by bending and stretching in the vicinity of the crack. It was also predicted that the radius of the crack blunting region can extend to lengths of up to 20 unit cells for lattices with $\bar{\rho} = 0.01$ ⁴⁷. The lateral displacements calculated for each sample here did not reveal any elastic blunting, likely because the kagome nanolattices in this work contain hollow, non-slender tubes while the work of Fleck, et al. assumes solid, slender beams⁴⁷.

¹ Global deformation is governed by the failure of a single node for all samples, provided the sample compliances are comparable.

All nanolattices with $(a/w) \leq 0.23$ failed away from the notch with the peak load remaining constant at $F_{peak} \sim 2\text{mN}$; nanolattices with wider notches failed along the plane of the notch, orthogonal to the loading direction, and F_{peak} decreased with a concomitant increase in compliance. **Figure 21** summarizes the stress at failure as a function of relative notch size and outlines failure location property space.

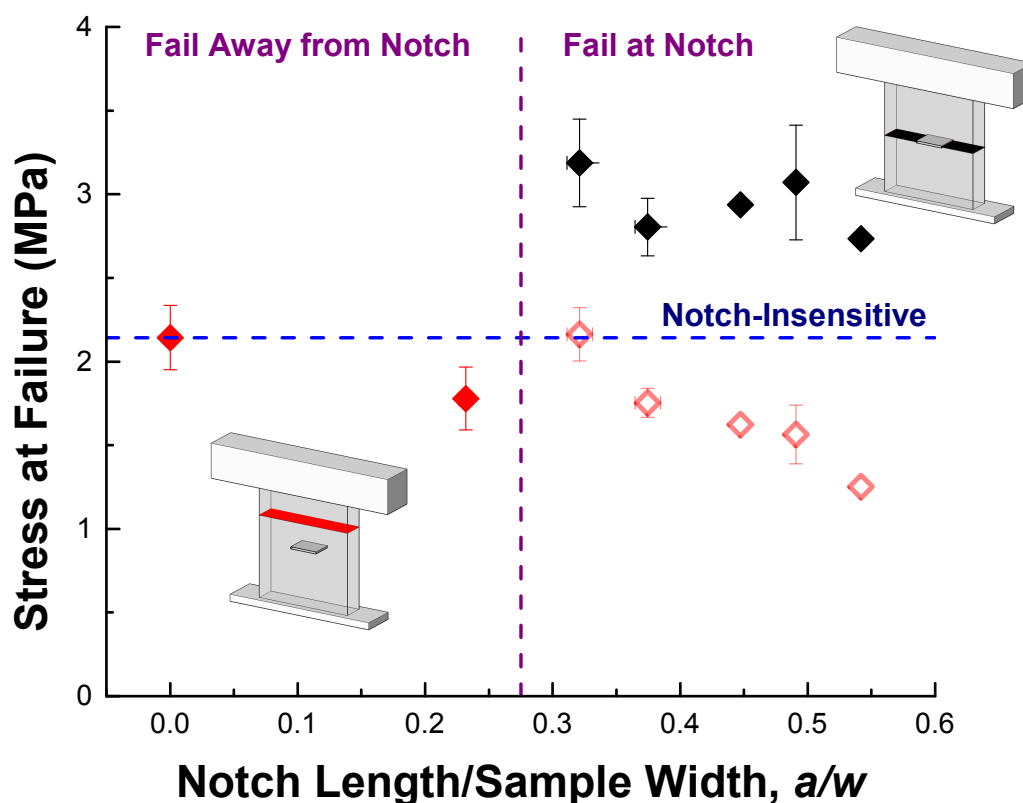


Figure 21: Stress at failure vs. the notch length to unit cell size ratio.

Solid symbols denote samples where the area used to normalize the load corresponds to the location of failure, whether at or away from the notch. Red symbols denote the peak load normalized by the total cross-sectional area of the tension specimen; black symbols denote the peak load normalized by the attached area at the notch plane. The blue dashed lined denotes the trend expected for a notch-insensitive material.

Failure stress was determined by dividing the peak load, F_{peak} , by the cross-sectional area, A , which was calculated using two different criteria: (1) the intact area at the plane of failure (black diamonds)^{4,5} and (2) the total cross-sectional area of the gauge section (red

diamonds). Using the first approach, we observed a roughly constant stress at failure of ~ 3 MPa for $(a/w) > 0.3$, a plateau that is consistent with literature^{4,5}. Using the intact area at the notch plane to calculate the stress at failure results in its increase by a factor of 1.8 when (a/w) increased from 0.23 to 0.32, which corresponds to a transition in failure location. A lower stress at failure of 2.73 MPa for the widest-spanning notch, $(a/w) = 0.54$, is likely a result of substantial compliance, 12.8 kPa^{-1} , of this sample. To determine the stress at failure for $(a/w) \geq 0.54$, samples with more unit cells across the width must be fabricated; the fabrication method used in this work poses limitations on creating significantly larger, structurally robust samples of the same geometry. When the stress at failure is calculated using the full cross-sectional area, a parameter space that is insensitive to flaws exists for $(a/w) < 0.38$ where the stress at failure is ~ 2.14 MPa. A reduction in stress at failure as (a/w) increases from 0.38 to 0.54, calculated using this method, stems from the higher sample compliance for $(a/w) > 0.38$, which wouldn't occur for larger samples with more unit cells spanning the un-notched region. This analysis demonstrates that hollow Al_2O_3 nanolattices are insensitive to the presence of external flaws for pre-fabricated defects spanning up to 50% of the sample width. We postulate that this flaw insensitivity arises from the discrete nature of the nanolattice at the micron scale such that the failure strength for notched and un-notched samples is governed by the failure strength of individual junctions between the unit cells subjected to uniaxial tension.

Figure 20 shows representative load-strain data for the notched and un-notched samples generated using FE simulations, which predict a 2.5-times lower peak load for the notched sample compared to the un-notched sample. The model predicted the same peak load as experimentally observed for the un-notched samples and severely under-predicted

it for the notched sample with $(a/w) = 0.32$ (Figures 19 and 20). We examined the sample region that contains the notch and the unit cell at the notch root, with the same region in the un-notched sample chosen as a reference for comparison. Figure 22 displays the von Mises stress distributions and associated distortions in the samples with $(a/w) = 0, 0.11$ and 0.35 at an applied nominal strain of $\varepsilon_y = 0.003$, which is well within the elastic regime of the deformation.

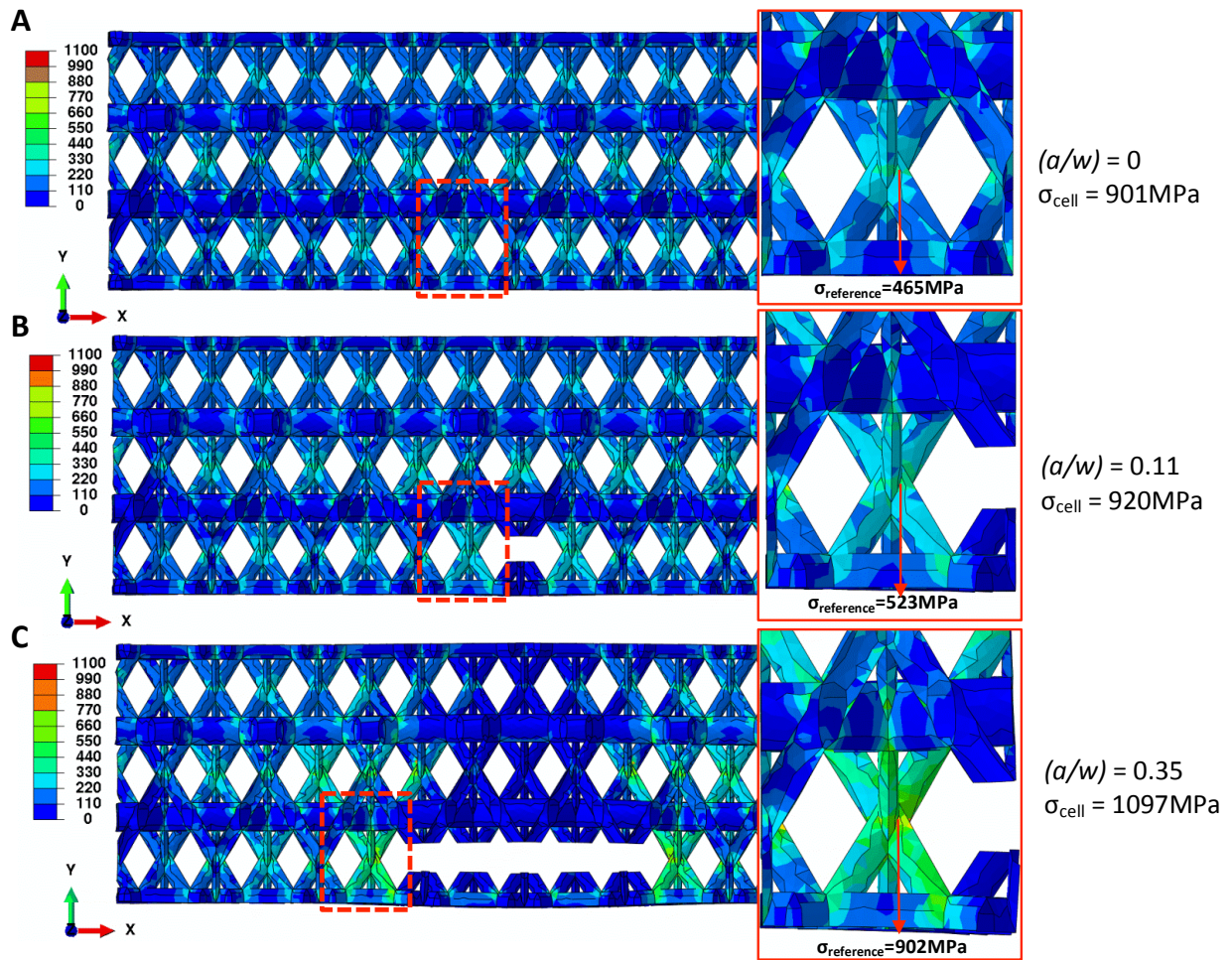


Figure 22: Contour plots of von Mises stress distributions in kagome lattice at a nominal strain of $\varepsilon_y = 0.003$ for $(a/w) = 0, 0.11$ and 0.35 .

The distortions shown are magnified by 5 times to enhance visualization. Insets are the close-up views of the unit cell at the notch root. σ_{node} denotes the von Mises stress at the same location on the junction node in the unit cell, and σ_{cell} refers to the maximum von Mises stress in the unit cell.

We denote $\sigma_{\text{reference}}$ as the von Mises stress at the junction node in the notch root unit cell, pointed to by the arrows in the zoomed view, and σ_{cell} as the maximum von Mises stress in the unit cell. Using the un-notched lattice, with $(a/w = 0)$, as a reference, simulations reveal that a short notch ($a/w = 0.11$) leads to the stress distributions and the associated distortions being comparable to those in the un-notched lattice. When the notch is lengthened to $(a/w) = 0.35$, the stresses in the unit cells above and below the notch become significantly lower, which generates a large stress concentration at the notch root. For the short notches, the relative change in $\sigma_{\text{reference}}$ is 13% and that in σ_{cell} is 2%; those for long notches are 94% and 22%, respectively. **Figure 22B** also shows that for the short-notch case, the distortions are marginal and similar to those in the un-notched samples, which corroborate the observed notch-insensitivity in experiments. For longer notches, the distortions become significant, with a shift in local stresses towards the notch roots. The insets in **Figure 22B** display a zoomed-in view of the notch root and show that for samples with a short notch, the node at the notch root experiences close-to-uniaxial tensile loading mode, which is similar to that in the samples without the notch (**Figure 22A**). In samples with long notches (**Figure 22C**), the node adjacent to the notch is subject to bending in addition to tension. Failure in long-notched samples initiates at the notch root node; the transition in stress state from tensile-only in the un- and short-notched samples to tensile-and-bending in the long-notched ones may cause different failure modes, which define the notch-insensitivity and notch-sensitivity regimes. The observed discrepancies between the computations and experimental results shown in **Figure 19** can be attributed to several factors. First, the compliance of the experimental setup cannot be accurately accounted for in the numerical simulations, which leads to a lower calculated peak loads. Secondly, the

beam wall thickness and diameter, as well as the hollowness of the beams in the gauge section and Al₂O₃/polymer composite in the sample head, are assumed to be perfectly uniform in the simulations, which is an idealization of the as-fabricated structure.

Additional calculations indicate that variations in tube wall thickness lead to a higher predicted peak load because of the greater load-bearing capacity of the trusses (See Supplementary Information). During sample preparation, the internal polymer of the sample head may be partially exposed to oxygen plasma near the kagome/octet interface, which would lead to variations in the stiffness of the sample head if the internal polymer inside is partially etched (See Supplementary Info). Our simulations revealed that the stress state at the notch root node changed from uniaxial tension to tension + bending with increasing notch length, which may render the maximum tensile stress-based failure criterion invalid. Several strategies are being pursued to improve the current numerical model, which include incorporating an inhomogeneous distribution of beam wall thicknesses by considering a statistical distribution of thicknesses based on experimental measurements, developing a better understanding of constituent material properties, and designing a more suitable failure criterion.

4.5 Conclusions

We fabricated 3-dimensional dog-bone shaped, hollow-beam alumina nanolattices with kagome architecture, with and without through-notches that span up to 50% of the sample width, and performed uniaxial tension experiments on them. These alumina nanolattices exhibit a nearly constant load-at-failure for notch length-to-sample width ratios of $(a/w) < 0.38$, which suggests insensitivity of failure to the presence of flaws. This is in contrast to failure of monolithic alumina containing a notch of comparable ratio, which

would necessarily fail at the notch at a significantly lower peak load compared to that of an un-notched specimen. We observed a reduction in the observed peak load for samples with $(a/w) \geq 0.38$ and attribute it to greater compliance of those samples, which stems from the fewer intact unit cells at the notch plane where failure occurs. We discovered that failure in these architected meta-materials is governed by the strength of the nodes, and that incipient failure occurs at the nodes with one un-constrained boundary. Once failure is initiated, the crack propagates instantaneously and catastrophically, as expected for a brittle material, along a plane of nodes orthogonal to the loading direction. These results suggest that nanolattices are insensitive to externally introduced defects because their failure mechanism is governed by the stress concentrations within the nodal geometry and by a transition from pure uniaxial tension to bending failure. These findings have significant implications in developing novel materials, which propels architected meta-materials to be particularly lucrative for applications that require simultaneous lightweight, strength, and damage tolerance.

Chapter 5: Summary and Future Work/Outlook of Structural Meta-Materials

This work presents the use of a novel two-photon fabrication technique to create hollow architected meta-materials, using both metallic and ceramic constituent materials. The mechanical responses of the nanolattices fabricated in this work are characterized using *in-situ* uniaxial compression and tension experiments.

Compression experiments were conducted on hollow gold octahedral nanolattices, with varying wall thicknesses and lattice angles, and demonstrated that structural and material size effects can be utilized to tune strength and stiffness. Higher lattice angles led to an increased instability of the lattice during the layer-by-layer collapse, but produced up to an order of magnitude increase in both strength and stiffness. Increasing the wall thickness of the hollow gold nanolattices leads to a change in the microstructure of the constituent gold film and this gives rise to an increased in yield strength by a factor of 2. In contrast to currently existing hollow metallic architected meta-materials, this work on the compression of hollow Au nanolattices demonstrates that the behavior of nanolattices cannot fully be described by a single mechanics-based theory, but additional theories accounting for the material strength as a function of microstructure must be employed to predict the behavior of the nanolattices.

A novel method was developed to fabricate 3-dimensional dog-boned shaped hollow alumina kagome nanolattice tension samples with a composite polymer/alumina octet-truss head. *In-situ* uniaxial tension experiments were performed on the hollow kagome test section by applying load along the bottom face of the octet-truss composite head and

observing both the load at the failure and the failure location. The kagome test sections were fabricated with notches spanning 0-50% of the sample width and the effect of notch length on peak load was observed. These alumina nanolattices exhibit a nearly constant load-at-failure for notch length-to-sample width ratios of $(a/w) < 0.38$, which suggests insensitivity of failure to the presence of flaws. This is in contrast to failure of monolithic alumina containing a notch of comparable ratio, which would necessarily fail at the notch at a significantly lower peak load compared to that of an un-notched specimen. For samples with larger (a/w) ratios, the peak load decreased with a concomitant increase in the compliance of the samples, which result from having fewer intact unit cells at the notch plane where failure occurs; a transition from purely tensile loading to tension + bending loading at the notch edge and this gives rise to lower observed peak loads at failure. We discovered that failure in these architected meta-materials is governed by the strength of the nodes, and that incipient failure occurs at the nodes with one un-constrained boundary. These findings have significant implications in developing novel materials, which propels architected meta-materials to be particularly lucrative for applications that require simultaneous lightweight, strength, and damage tolerance.

While great strides have been made in structural meta-materials, there still exists a challenge to create meta-materials with components at the nanometer length scale using scalable processes. The most significant obstacle today to utilizing structural meta-materials in useful technological applications is scalability, i.e., manufacturing either a large number of small-scale components or materials with large dimensions in a reasonable amount of time. Some of the possible technologies that could lead to a scalable route for producing small-featured metal-materials include roll-to-roll fabrication with nano-

imprintable patterns, holographic lithography, and phase-shifting masks. Once new techniques are developed to make scalable nanolattice samples, it will be possible to further explore the flaw tolerance demonstrated by the small-scale samples of this work. Additionally, larger samples will make it possible to determine the fracture toughness of these inherently discrete nanolattices and address fundamental questions, such as when discrete materials begin to behave as continuum materials and how nanoscale size effects can be proliferated onto bulk materials.

Appendices

Appendix A: Laser Power Exposure Test Matrix

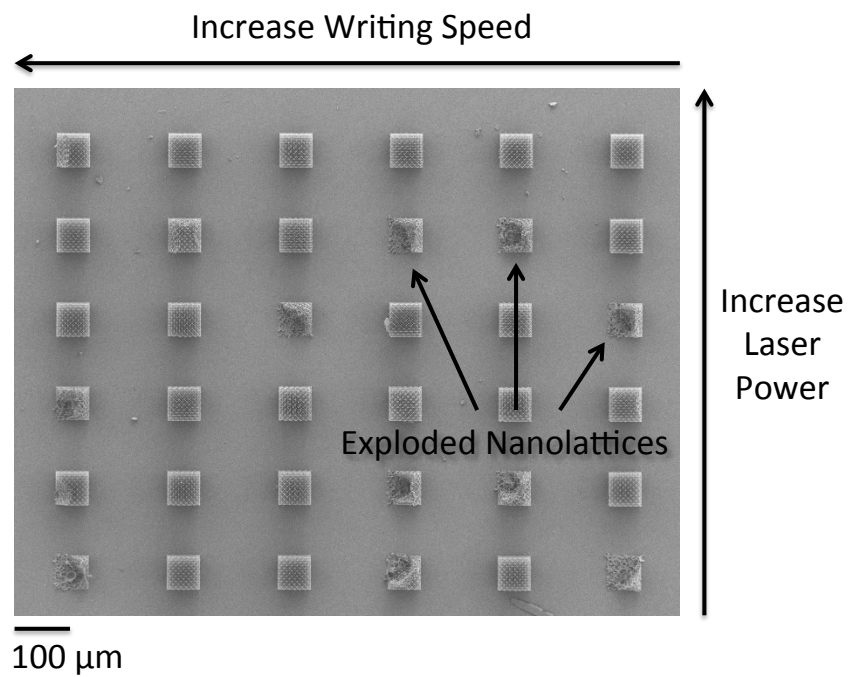


Figure 23: Small -scale explosions are observed when the laser power is sufficiently high.

Appendix B: Representative Images of Etched and Non-Etched Samples

The samples are imaged at 5-10kV to non-destructively determine the amount of polymer that has been removed. **Figure 24** shows a representative sample that shows the location of the polymer, which is denoted by a change in contrast of the sample. Samples were etched in O₂ plasma for a total of 16-18 hours, depending on the notch length, and checked for hollowness every 4-6 hours.

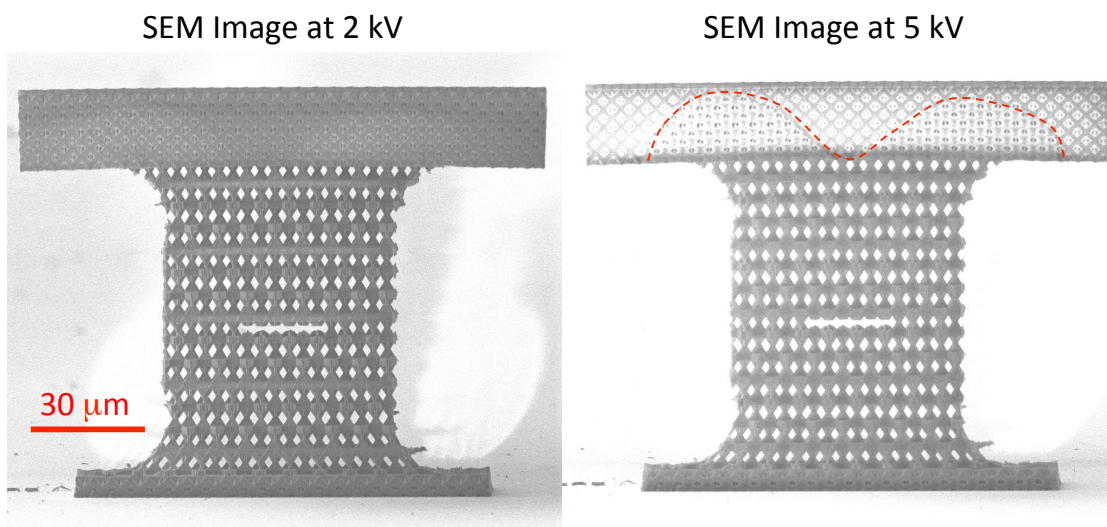


Figure 24: Representative images of polymer etching using different SEM voltages; the red dotted line indicated the etch front of the O₂ plasma in the octet-truss head.

Appendix C: Calculation of Stiffness for Grip and Test Gauge Sections

The strength and stiffness of a stretching-dominated cellular solid, such as the octet-truss lattice, scale linearly with the modulus and relative density $\bar{\rho}$, where $\bar{\rho}$ is the ratio between the volume of lattice the unit cell normalized by the total volume occupied by the unit cell^{41,84}. These theories assume long, slender, solid bars with rigid nodal connections, though many lightweight foams are made with techniques that produce hollow bars and nodes^{33,29,39}. The hollow kagome test sections in this work have a relative density of $\bar{\rho} = 0.02$ and the octet-truss grips have a relative density of $\bar{\rho} = 0.38$. The relative densities are estimated from Solidworks model assuming a constant, perfectly 50nm conformal coating of Al_2O_3 and either hollow (kagome test section) or filled (octet-truss grips) lattice tubes. The SolidWorks model assumes a unit cell size of $l = 3.85\mu\text{m}$ for the kagome test section and $l = 4.5\mu\text{m}$ for the octet-truss grips. The dimensions of the voxel, which are used to trace the lattice geometry, have a semi-major axis of $a = 1.8\mu\text{m}$ and semi-minor axis of $b = 0.5\mu\text{m}$. These voxel dimensions were determined by measuring the voxel for a variety of laser power settings for the two-photon lithography process.

The relationship between relative density and stiffness of the hollow kagome lattices was determined using cyclic nano-indentation (G200) in the elastic regime of samples with dimensions of $4 \times 5 \times 3$ unit cells in size at a quasi-static strain rate of $\dot{\epsilon} = 10^{-3}\text{s}^{-1}$. The lattice unit cell sizes was $l = 3.5\mu\text{m}$, the wall thicknesses of the Al_2O_3 coating was 50nm, and the angle of the kagome unit cells was $\theta = 54.7^\circ$. The relative density of the hollow kagome nanolattice was determined to be from $\bar{\rho} = 0.02$, similar to those tested in uniaxial tension in this work. Three cycles were used and the modulus is estimated from the stress-strain loading curve when the displacement does not exceed the elastic limit, as

shown in **Figure 25**. The stiffness of the hollow kagome lattice is approximated to be

$$E_{kagome} = 45 \text{ MPa.}$$

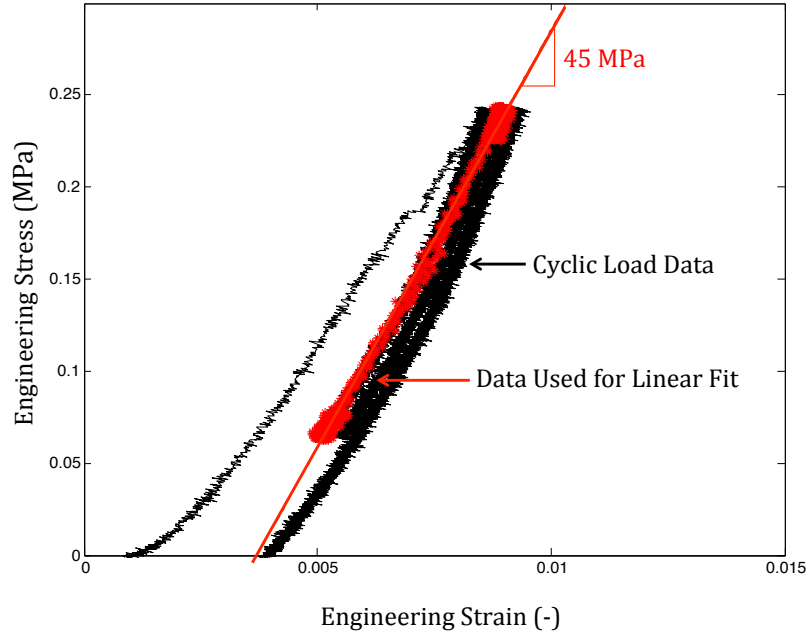


Figure 25: Engineering stress-strain curve for compressive stiffness of 54.7° 3D kagome nanolattices.

The stiffness of the octet-truss grip is calculated using the analytic scaling for a stretching-dominated structure, where $E_{Octet-truss} = 0.3 E_{bulk} \bar{\rho}^{22,41}$. The stiffness E_{bulk} is estimated using the rule-of-mixtures for composites, where

$$E_{bulk} = v_{f, polymer} E_{polymer} + v_{f, Al2O3} E_{Al2O3}$$

The volume fractions are calculated using the SolidWorks model and are found to be:

$$v_{total} = 47.3 \text{ } \mu\text{m}^3$$

$$v_{polymer} = 38.0 \text{ } \mu\text{m}^3$$

$$v_{Al2O3} = 9.31 \text{ } \mu\text{m}^3$$

$$v_{f, Al2O3} = (v_{total} - v_{polymer})/v_{total} = 0.18$$

$$v_{f, polymer} = (v_{total} - v_{Al_2O_3})/v_{total} = 0.80$$

The bulk material properties of the polymer were found via quasi-static nano-indentation experiments and determined to be $E_{polymer} = 2.1$ GPa by Meza, et. al.

This gives an estimated E_{bulk} for the composite Al_2O_3 /polymer octet-truss bulk material to be:

$$E_{bulk} = E_{polymer} v_{polymer} + E_{Al_2O_3} v_{Al_2O_3}$$

$$E_{bulk} = 34.2 \text{ GPa}$$

Using the analytic solution for the stiffness of an octet-truss with solid lattice members, the stiffness of the grips is calculated to be:

$$E_{Octet-truss} = 0.3 E_{bulk} \bar{\rho}$$

$$E_{Octet-truss} = 3.90 \text{ GPa}$$

Appendix D: Elastic Blunting Phenomena in 3D Hollow Kagome Nanolattices

Fleck et. al. predict that the elastic blunting phenomena of the 2D kagome lattice appear in bands of high strain emanating from the notch tip²⁶. If elastic blunting occurred for the 3D kagome nanolattice plates in this work, we would expect similar banding behavior emanating from the crack tip; however, none is observed, as shown in **Figure 26**.

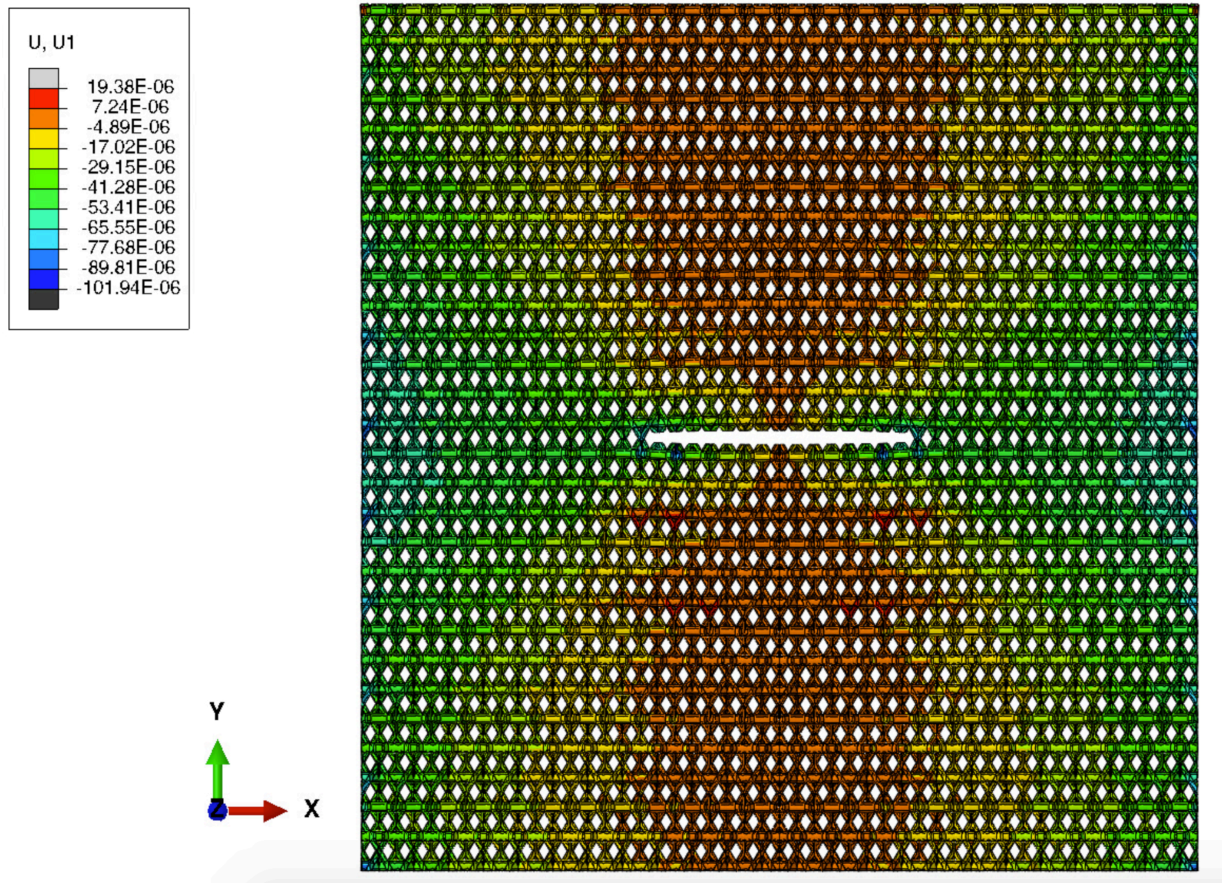


Figure 26: No elastic crack tip blunting is localized near the crack tip for the 3D kagome nanolattice plates; all deformation in the x-direction is localized near the middle of the sample at the moment prior to failure.

Appendix E: Peak Load for Variation in Wall Thicknesses

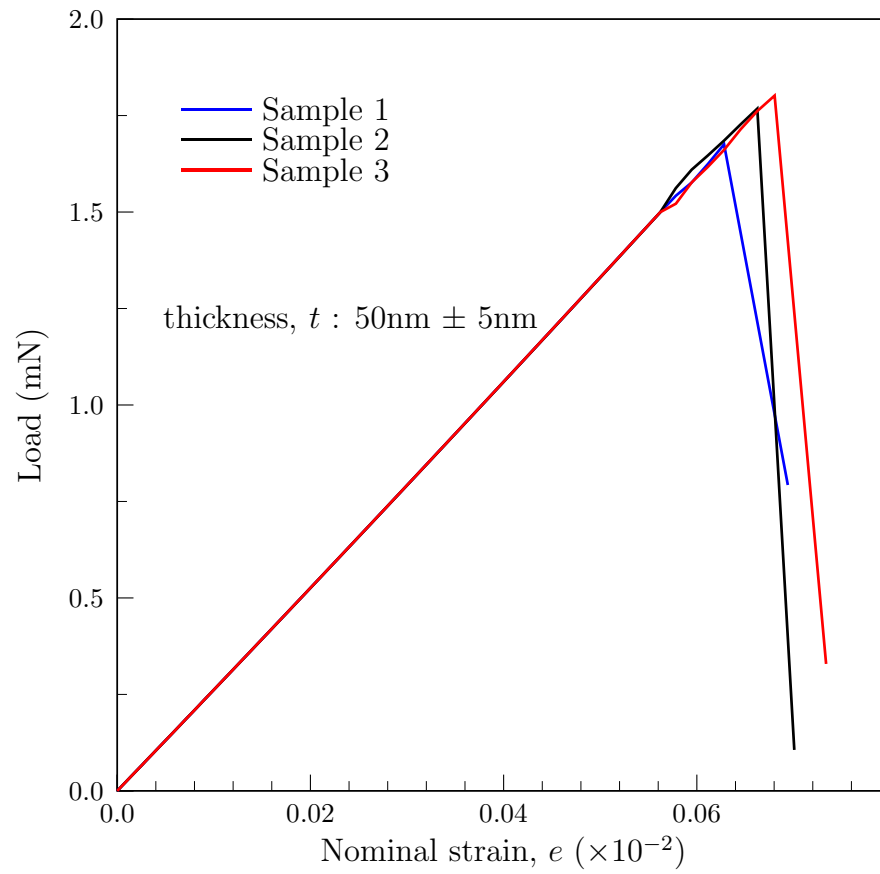


Figure 27: Variations in wall thickness give rise to higher peak loads.

References

1. Jennings, A. T., Burek, M. J. & Greer, J. R. Microstructure versus Size: Mechanical Properties of Electroplated Single Crystalline Cu Nanopillars. *Phys. Rev. Lett.* **104**, 135503 (2010).
2. Greer, J. R. & De Hosson, J. T. M. Plasticity in small-sized metallic systems: Intrinsic versus extrinsic size effect. *Prog. Mater. Sci.* **56**, 654–724 (2011).
3. Greer, J. R. & Nix, W. D. Size dependence of mechanical properties of gold at the sub-micron scale. *Appl. Phys. A* **80**, 1625–1629 (2005).
4. Greer, J. R., Oliver, W. C. & Nix, W. D. Size dependence of mechanical properties of gold at the micron scale in the absence of strain gradients. *Acta Mater.* **53**, 1821–1830 (2005).
5. Dou, R. & Derby, B. A universal scaling law for the strength of metal micropillars and nanowires. *Scr. Mater.* **61**, 524–527 (2009).
6. Greer, J. R., Jang, D. & Gu, X. W. Exploring Deformation Mechanisms in Nanostructured Materials. *J. Mater.* **64**, 1241–1252 (2012).
7. Dietiker, M., Buzzi, S., Pigozzi, G., Löffler, J. F. & Spolenak, R. Deformation behavior of gold nano-pillars prepared by nanoimprinting and focused ion-beam milling. *Acta Mater.* **59**, 2180–2192 (2011).
8. Volkert, C. A. & Lilleodden, E. T. Size effects in the deformation of sub-micron Au columns. *Philos. Mag.* **86**, 5567–5579 (2006).
9. Oh, S. H., Legros, M., Kiener, D. & Dehm, G. In situ observation of dislocation nucleation and escape in a submicrometre aluminium single crystal. *Nat. Mater.* **8**, 95–100 (2009).
10. Jang, D. & Greer, J. R. Size-induced weakening and grain boundary-assisted deformation in 60 nm grained Ni nanopillars. *Scr. Mater.* **64**, 77–80 (2011).
11. Gu, X. W. *et al.* Size-dependent deformation of nanocrystalline Pt nanopillars. *Nano Lett.* **12**, 6385–92 (2012).
12. Yang, B., Motz, C., Rester, M. & Dehm, G. Yield stress influenced by the ratio of wire diameter to grain size – a competition between the effects of specimen microstructure and dimension in micro-sized polycrystalline copper wires. *Philos. Mag.* **92**, 3243–3256 (2012).

13. Rys, J. *et al.* Fabrication and Deformation of Metallic Glass Micro-Lattices. *Adv. Eng. Mater.* 889–896 (2014). doi:10.1002/adem.201300454
14. Chen, D. Z. *et al.* Nanometallic glasses: size reduction brings ductility, surface state drives its extent. *Nano Lett.* **13**, 4462–8 (2013).
15. Chen, C. Q., Pei, Y. T. & De Hosson, J. T. M. Effects of size on the mechanical response of metallic glasses investigated through in situ TEM bending and compression experiments. *Acta Mater.* **58**, 189–200 (2010).
16. Volkert, C. A., Donohue, A. & Spaepen, F. Effect of sample size on deformation in amorphous metals. *J. Appl. Phys.* **103**, 083539 (2008).
17. Wang, J., Evans, A. G., Dharmasena, K. & Wadley, H. N. G. On the performance of truss panels with Kagomé cores. *Int. J. Solids Struct.* **40**, 6981–6988 (2003).
18. Wadley, H. N. G., Fleck, N. & Evans, A. G. Fabrication and structural performance of periodic cellular metal sandwich structures. *Compos. Sci. Technol.* **63**, 2331–2343 (2003).
19. Chiras, S. *et al.* The structural performance of near-optimized truss core panels. *Int. J. Solids Struct.* **39**, 4093–4115 (2002).
20. Deshpande, V. . & Fleck, N. . Collapse of truss core sandwich beams in 3-point bending. *Int. J. Solids Struct.* **38**, 6275–6305 (2001).
21. Deshpande, V. S., Ashby, M. F. & Fleck, N. A. Foam topology: bending versus stretching dominated architectures. *Acta Mater.* **49**, 1035–1040 (2001).
22. Fleck, N. A., Deshpande, V. S. & Ashby, M. F. Micro-architected materials: past, present and future. *Proc. R. Soc. A Math. Phys. Eng. Sci.* **466**, 2495–2516 (2010).
23. Deshpande, V. S., Fleck, N. A. & Ashby, M. F. Effective properties of the octet-truss lattice material. *J. Mech. Phys. Solids* **49**, 1747–1769 (2001).
24. Hutchinson, R. G. & Fleck, N. A. The structural performance of the periodic truss. *J. Mech. Phys. Solids* **54**, 756–782 (2006).
25. Symons, D. D. & Fleck, N. a. The Imperfection Sensitivity of Isotropic Two-Dimensional Elastic Lattices. *J. Appl. Mech.* **75**, 051011 (2008).
26. Fleck, N. a. & Qiu, X. The damage tolerance of elastic–brittle, two-dimensional isotropic lattices. *J. Mech. Phys. Solids* **55**, 562–588 (2007).
27. Hodge, A. M. *et al.* Monolithic nanocrystalline Au fabricated by the compaction of nanoscale foam. *J. Mater. Res.* **20**, 554–557 (2005).

28. Bauer, J., Hengsbach, S., Tesari, I., Schwaiger, R. & Kraft, O. High-strength cellular ceramic composites with 3D microarchitecture. *Proc. Natl. Acad. Sci. U. S. A.* **111**, 2453–8 (2014).
29. Schaedler, T. A. *et al.* Ultralight metallic microlattices. *Science* **334**, 962–5 (2011).
30. Montemayor, L. C. & Greer, J. R. Mechanical Response of Hollow Metallic Nanolattices: Combining Structural and Material Size Effects. *J. Appl. Mech.* **82**, (2015).
31. Meza, L. R., Das, S. & Greer, J. R. Strong, lightweight, and recoverable three-dimensional ceramic nanolattices. *Science (80-.).* **345**, 1322–1326 (2014).
32. Gu, X. W. & Greer, J. R. Ultra-Strong Architected Cu Meso-lattices. *Extrem. Mech. Lett.* **2**, 7–14 (2015).
33. Zheng, X. *et al.* Ultralight, ultrastiff mechanical metamaterials. *Science (80-.).* **344**, 1373–1377 (2014).
34. Jacobsen, A. J., Barvosa-Carter, W. & Nutt, S. Micro-scale Truss Structures formed from Self-Propagating Photopolymer Waveguides. *Adv. Mater.* **19**, 3892–3896 (2007).
35. Fischer, J. & Wegener, M. Three-dimensional optical laser lithography beyond the diffraction limit. *Laser Photon. Rev.* **7**, 22–44 (2013).
36. Sun, H. & Kawata, S. Two-photon photopolymerization and 3D lithographic microfabrication. *Am. Phys. Soc.* 169–274 (2004). doi:10.1007/b94405
37. Xiong, W. *et al.* Simultaneous additive and subtractive three-dimensional nanofabrication using integrated two-photon polymerization and multiphoton ablation. *Light Sci. Appl.* **1**, e6 (2012).
38. Jacobsen, A. J., Barvosa-Carter, W. & Nutt, S. Micro-scale truss structures with three-fold and six-fold symmetry formed from self-propagating polymer waveguides. *Acta Mater.* **56**, 2540–2548 (2008).
39. Montemayor, L. C., Meza, L. R. & Greer, J. R. Design and Fabrication of Hollow Rigid Nanolattices via Two-Photon Lithography. *Adv. Eng. Mater.* **16**, 184–189 (2014).
40. Torrents, A., Schaedler, T. A., Jacobsen, A. J., Carter, W. B. & Valdevit, L. Characterization of nickel-based microlattice materials with structural hierarchy from the nanometer to the millimeter scale. *Acta Mater.* **60**, 3511–3523 (2012).
41. Gibson, L. J. & Ashby, M. F. *Cellular Solids: Structure and Properties*. (Cambridge University Press, 1999).

42. Maloney, K. J. *et al.* Microlattices as architected thin films: Analysis of mechanical properties and high strain elastic recovery. *APL Mater.* **1**, 022106 (2013).
43. Valdevit, L., Godfrey, S. W., Schaedler, T. A., Jacobsen, A. J. & Carter, W. B. Compressive strength of hollow microlattices: Experimental characterization, modeling, and optimal design. *J. Mater. Res.* **28**, 2461–2473 (2013).
44. Jang, D., Meza, L., Greer, F. & Greer, J. Fabrication and deformation of three-dimensional hollow ceramic nanostructures. *Nat. Mater.* **12**, 893–898 (2013).
45. Meza, L. R. & Greer, J. R. Mechanical characterization of hollow ceramic nanolattices. *J. Mater. Sci.* **49**, 2496–2508 (2014).
46. Gu, X. W. *et al.* Mechanisms of Failure in Nanoscale Metallic Glass. *Nano Lett.* (2014). doi:10.1021/nl5027869
47. Wallach, J. C. & Gibson, L. J. Mechanical behavior of a three-dimensional truss material. *Int. J. Solids Struct.* **38**, 7181–7196 (2001).
48. Ng, K. Y., Lin, Y. & Ngan, a. H. W. Deformation of anodic aluminum oxide nano-honeycombs during nanoindentation. *Acta Mater.* **57**, 2710–2720 (2009).
49. Hodge, A. M. *et al.* Scaling equation for yield strength of nanoporous open-cell foams. *Acta Mater.* **55**, 1343–1349 (2007).
50. Valdevit, L., Jacobsen, A. J., Greer, J. R. & Carter, W. B. Protocols for the Optimal Design of Multi-Functional Cellular Structures: From Hypersonics to Micro-Architected Materials. *J. Am. Ceram. Soc.* **94**, s15–s34 (2011).
51. Lian, J. *et al.* Catastrophic vs Gradual Collapse of Thin-Walled Nanocrystalline Ni. 4118–4125 (2011).
52. LaFratta, C. N., Fourkas, J. T., Baldacchini, T. & Farrer, R. a. Multiphoton fabrication. *Angew. Chem. Int. Ed. Engl.* **46**, 6238–58 (2007).
53. Jeon, S., Malyarchuk, V., Rogers, J. A. & Wiederrecht, G. P. Fabricating three-dimensional nanostructures using two photon lithography in a single exposure step. *Opt. Express* **14**, 2300–8 (2006).
54. Sun, H.-B., Matsuo, S. & Misawa, H. Three-dimensional photonic crystal structures achieved with two-photon-absorption photopolymerization of resin. *Appl. Phys. Lett.* **74**, 786–788 (1999).
55. Tétreault, N. *et al.* New Route to Three-Dimensional Photonic Bandgap Materials: Silicon Double Inversion of Polymer Templates. *Adv. Mater.* **18**, 457–460 (2006).

56. Thornton, J. A. Influence of substrate temperature and deposition rate on structure of thick sputtered Cu coatings. *J. Vac. Sci. Technol.* **12**, 830–835 (1975).
57. Thornton, J. A. The microstructure of sputter-deposited coatings. *J. Vac. Sci. Technol. A Vacuum, Surfaces, Film.* **4**, 3059–3065 (1986).
58. Thornton, J. A. Influence of apparatus geometry and deposition conditions on the structure and topography of thick sputtered coatings. *J. Vac. Sci. Technol.* **11**, 666–670 (1974).
59. Valdevit, L. *Personal Communications*.
60. Oliver, W. & Pharr, G. An improved technique for determining hardness and elastic modulus using load and displacement sensing indentation experiments experiments. *J. Mater. Res.* 1564–1583 (1992).
61. C. V. Thompson. Structure Evolution During Processing of Polycrystalline Films. *Annu. Rev. Mater. Sci.* **30**, 159–190 (2000).
62. Koller, A. *et al. Structure and Properties of Ceramics*. (Elsevier, 1994).
63. Gross, D. & Seelig, T. *Fracture Mechanics with an Introduction to Micromechanics*. (Springer, 2011).
64. Lawn, B. *Fracture of Brittle Solids*. (Cambridge University Press, 1993).
65. McNulty, J. C., Zok, F. W., Genin, G. M. & Evans, A. G. Notch-Sensitivity of Fiber-Reinforced Ceramic-Matrix Composites: Effects of Inelastic Straining and Volume-Dependent Strength. *J. Am. Ceram. Soc* **82**, 1217–1245 (1999).
66. Mackin, T. J., Purcell, T. E., He, M. Y. & Evans, A. G. Notch Sensitivity and Stress Redistribution in Three Ceramic-Matrix Composites. (1995).
67. Heredia, F. E. *et al.* Notch effects in carbon matrix composites. *J. Am. Ceram. Soc* **77**, 2817–2927 (1995).
68. Cady, C., Mackin, T. & Evans, A. Silicon Carbide/Calcium Aluminosilicate: A Notch-Insensitive Ceramic-Matrix Composite. *J. Am. Ceram. Soc.* **78**, 77–82 (1995).
69. Arzt, E., Fratzl, P., Gao, H., Ji, B. & Ja, I. L. Materials become insensitive to flaws at nanoscale : **100**, 5597–5600 (2003).
70. Gu, X. W., Wu, Z., Zhang, Y.-W., Srolovitz, D. J. & Greer, J. R. Microstructure versus flaw: mechanisms of failure and strength in nanostructures. *Nano Lett.* **13**, 5703–9 (2013).

71. Wu, Z. X., Zhang, Y. W., Jhon, M. H., Greer, J. R. & Srolovitz, D. J. Nanostructure and surface effects on yield in Cu nanowires. *Acta Mater.* **61**, 1831–1842 (2013).
72. Jennings, A. T., Burek, M. J. & Greer, J. R. Microstructure versus Size: Mechanical Properties of Electroplated Single Crystalline Cu Nanopillars. *Phys. Rev. Lett.* **104**, 135503 (2010).
73. J. S. Huang, L. J. G. Fracture toughness of brittle honeycombs. *Acta Metall. Mater.* **39**, 1617–1626 (1991).
74. Huang, J. S. & Gibson, L. J. Fracture toughness of brittle foams. *Acta Metall. Mater.* **39**, 1627–1636 (1991).
75. Brezny, R. & Green, D. J. Fracture Behavior of Open-Cell Ceramics. **52**, (1989).
76. Brezny, R. & Green, D. J. Factors Controlling the Fracture Resistance of Brittle Cellular Materials. **65**, 1061–1065 (1991).
77. Choi, S. & Sankar, B. V. A micromechanical method to predict the fracture toughness of cellular materials. *Int. J. Solids Struct.* **42**, 1797–1817 (2005).
78. Romijn, N. E. R. & Fleck, N. A. The fracture toughness of planar lattices: Imperfection sensitivity. *J. Mech. Phys. Solids* **55**, 2538–2564 (2007).
79. Quintana-Alonso, I., Mai, S. P., Fleck, N. A., Oakes, D. C. H. & Twigg, M. V. The fracture toughness of a cordierite square lattice. *Acta Mater.* **58**, 201–207 (2010).
80. Maiti, S. K., Ashby, M. F. & Gibson, L. J. Fracture Toughness of Brittle Cellular Solids. *Scr. Mater.* **18**, 213–217 (1984).
81. Berdova, M. *et al.* Mechanical assessment of suspended ALD thin films by bulge and shaft-loading techniques. *Acta Mater.* **66**, 370–377 (2014).
82. Wachtman, J. B. *Mechanical Properties of Ceramics*. (John Wiley & Sons, Inc., 1996).
83. Griffith, A. A. The Phenomena of Rupture and Flow in Solids. *Philos. Trans. R. Soc. London. Ser. A, Contain. Pap. a Math. or Phys. Character* **221**, 163–198 (1921).
84. Ashby, M. F. The properties of foams and lattices. *Philos. Trans. A. Math. Phys. Eng. Sci.* **364**, 15–30 (2006).